atmosphere

Article

A Spatially Detailed Projection of Environmental Conditions in the Arctic Initiated by Climate Change

Alexander Kislov *, Ali Alyautdinov, Alisa Baranskaya, Nataliya Belova, Daria Bogatova, Marina Vikulina, Irina Zheleznova and Galina Surkova

Faculty of Geography, Lomonosov Moscow State University, Leninskie Gory MGU, GSP-1, 119991 Moscow, Russia
* Correspondence: avkislov@mail.ru; Tel.: +7-495-939-3043

Abstract: The environmental conditions of the Arctic are vulnerable to the effects of climate change. We focus on the territory of the Yamalo-Nenets Autonomous Okrug (YaNAO). The objective of this study is to project mid-21st century climate-driven changes in the state of climate and the natural environment in the YaNAO. For this purpose, the CMIP6 data models with the climate change scenario SSP5-8.5 were used. Climate change directly affects the statistics of extreme events and climatically driven phenomena, such as frosts and thaws, as well as avalanches and slush flows. Climate change causes changes in the Arctic environment, primarily due to permafrost degradation, leading to important modifications in events such as mudflows, cryogenic landslides, abrasion, erosion, suffusion, frost heave, solifluction, thermokarst, and others. In some cases, the intensity and area of these processes increase, such as heaving processes and thermokarst becoming more active by 2050. In other cases, the solifluction processes decrease in the south part of the YaNAO due to the discontinuous or sporadic permafrost distribution. Projected climatic changes will inevitably lead to the restructuring of the geosystems in YaNAO, creating risks for infrastructure in economically active territories.

Keywords: Arctic warming; frosts and thaws; avalanches and slush flows; mudflows; cryogenic landslides; erosion; suffusion; frost heave; solifluction; thermokarst

Citation: Kislov, A.; Alyautdinov, A.; Baranskaya, A.; Belova, N.; Bogatova, D.; Vikulina, M.; Zheleznova, I.; Surkova, G. A Spatially Detailed Projection of Environmental Conditions in the Arctic Initiated by Climate Change. *Atmosphere* **2023**, *14*, 1003. https://doi.org/10.3390/atmos14061003

Academic Editor: Jean-Christophe Raut

Received: 27 April 2023
Revised: 29 May 2023
Accepted: 7 June 2023
Published: 9 June 2023

1. Introduction

The sixth Assessment Report (AR6) of the Intergovernmental Panel on Climate Change (IPCC) reported a trend of climate conditions at the country scale in the Arctic, where the area has warmed more quickly than any other region on Earth. This increase in the annual and seasonal mean temperature is the so-called Arctic amplification [1], which results from the intensification of poleward heat advection [2,3] and the "Arctic Atlantification" within the upper layer of the ocean [4], with the participation of feedbacks of temperature and sea ice [5,6].

The environmental conditions of the Arctic are highly vulnerable to the effects of climate change; however, these influences differ across Arctic regions. We focus on the territory of the Yamalo-Nenets Autonomous Okrug (YaNAO), which is located near the convergence of 70 N and 70 E (see maps below). The area consists of Arctic tundra and northern taiga, with three large peninsulas - the Yamal Peninsula, the Taz Peninsula, and the Gyda Peninsula which together represent the Arctic coastal lowlands of northwestern Siberia. There are nearly 300,000 lakes in the area, and the Polar Urals rise in the western part, which is the highest region of the YaNAO. The Ob River flows through YaNAO to the Kara Sea via the Gulf of Ob, which dominates the geography of the YaNAO. A number of islands are located off the YaNAO coast.

Climatic features of the European Arctic are primarily determined by the influence of the northern part of the Atlantic Ocean. However, the YaNAO is located much farther east, and here the influence of the Atlantic is combined with the Arctic processes determined by the Kara Sea, which is covered with ice during most of the year [7], and the continentality of the climate intensifies to the east. Notably, relatively little research has been published regarding the climate of this region, which is an area of intensive shipping, fishery, and the largest hydrocarbon (petroleum and natural gas) basin in the world's natural gas production.

Climate change directly affects the statistics of extreme events [8,9] and climatically driven phenomena, such as frosts and thaws [10], as well as avalanches and slush flows [11]. In combination with climatically-induced permafrost destruction, these changes can lead to important modifications in events, such as mudflows, cryogenic landslides [12], abrasion [13,14], erosion [15], suffusion [16], frost heave [17], solifluction [18], thermokarst [19], and others.

The objective of this study is to project mid-21st century climate-driven changes in the state of the natural environment in the YaNAO. This task can be accomplished by assessing whether climate changes, as reproduced by climate models, can cause changes in environmental properties and by determining the magnitude of such changes. For this purpose, the CMIP6 data models with the climate change scenario SSP5-8.5 were used. Its selection does not limit the generality of the obtained results, as the differences in anomalies corresponding to different scenarios of SSPs are statistically indistinguishable until approximately the middle of the century. Specific subject-oriented models are then required to transition from climate change to changes in certain indicators of the environment. These models are a set of algorithms that allow for the conversion of climate variables to environmental characteristics.

In the considered relatively small and flat area, the mosaic pattern of climatic anomalies is associated with soil and plant parameters.

In the following section, we briefly describe the study area and summarize information regarding the method of climate change projection. The next section provides evidence that Weibull and Gauss probability distributions can be used to calculate the projection of quantile values. In subsequent sections, we describe the climatically-induced response of different properties and processes, such as thaws, avalanches, cryogenic landslides, etc. The last section concludes the paper.

2. Materials and Methods

The study was conducted in the sub-Arctic region of the YaNAO, which includes both coastal and inland areas. The study utilized a dataset of monthly temperature and precipitation data for the period 1966–2018 from meteorological stations located within the region (Table 1). The locations of these stations are shown in all figures.

Table 1. Meteorological stations across the YaNAO (http://meteo.ru/, accessed on 1 January 2020).

Station	Lat., N	Lon., E
Popova station	73°19′	70°3′
Marresale	69°42′	66°48′
Antipayuta	69°06′	76°51′
Tazovsk	67°26′	78°42′
Salekhard	66°32′	66°38′
Novy Port	67°41′	72°53′
Nyda	66°36′	72°55′
Nadym	65°32′	72°31′
Tarko-Sale	64°55′	77°46′
Chalasavei	63°23′	78°19′
Tolka	64°00′	82°03′

Additionally, a dataset of climate simulations from CMIP6 (Coupled Model Intercomparison Project, Phase 6) models [20] for the period 2015–2065 was used (Table 2). The data for the YaNAO and adjacent regions (60°–75° N, 60°–90° E) were extracted from the global data of each climate model, interpolated onto a 1° × 1° deg. Lat. × Long. grid and intermodal averaged. The projection was made for the period 2035–2065 based on the SSP5-8.5 scenario, which corresponds to the mid-21st century climate. The predicted change in the value X was determined in two stages. Firstly, the anomaly X_{eb}^{model} was calculated from the model data using Equation (1),

$$X_{eb}^{model} = X_{e}^{model} - X_{b}^{model} \quad (1)$$

Here, X_{e}^{model} and X_{b}^{model} represent the simulated values for the projected interval (2035–2065) and the base interval (2015–2025), respectively.

In the second stage, the predictive value (X_e) was calculated using the correction of the known value from current data as shown in Equation (2), where

$$X_e = X_b^{curr} + X_{eb}^{model}, \quad (2)$$

where both observation and reanalysis data were used to assess the current value X_b^{curr}.

The ERA5 re-analysis developed by ECMWF [21] was used as a source of current data for the period 1995–2015. It reflects the conditions of the "pause" in global warming followed by a period of rapid warming acceleration in the late 20th century. The reanalysis data were interpolated to the same $1° \times 1°$ grid for comparability with the CMIP6 model data.

Table 2. List of models of the CMIP6 project, the data of which were used to calculate the climatic parameters of the YaNAO.

#	Model	Country	Grid Step	#	Model	Country	Grid Step
1	ACCESS-CM2	Australia	$1.88° \times 1.24°$	22	GFDL-ESM4	USA	$1.25° \times 1°$
2	ACCESS-ESM1-5	Australia	$1.88° \times 1.25°$	23	GISS-E2-1-G	USA	$2.50° \times 2°$
3	AWI-CM-1-1-MR	Germany	$0.94° \times 0.94°$	24	HadGEM3-GC31-LL	United Kingdom	$1.88° \times 1.25°$
4	BCC-CSM2-MR	China	$1.13° \times 1.13°$	25	HadGEM3-GC31-MM	United Kingdom	$0.83° \times 0.56°$
5	CAMS-CSM1-0	China	$1.13° \times 1.13°$	26	IITM-ESM	India	$1.88° \times 1.91°$
6	CanESM5	Canada	$2.81° \times 2.81°$	27	INM-CM4-8	Russia	$2° \times 1.5°$
7	CanESM5-CanOE	Canada	$2.81° \times 2.81°$	28	INM-CM5-0	Russia	$2° \times 1.5°$
8	CAS-ESM2-0	China	$1.41° \times 1.41°$	29	IPSL-CM6A-LR	France	$2.5° \times 1.26°$
9	CESM2-WACCM	USA	$1.25° \times 0.94°$	30	KACE-1-0-G	Korea	$1.88° \times 1.25°$
10	CIESM	China	$1.25° \times 0.94°$	31	KIOST-ESM	Korea	$1.88° \times 1.88°$
11	CMCC-CM2-SR5	Italy	$1.25° \times 0.94°$	32	MCM-UA-1-0	USA	$3.75° \times 2.25°$
12	CMCC-ESM2	Italy	$1.25° \times 0.94°$	33	MIROC6	Japan	$1.41° \times 1.41°$
13	CNRM-CM6-1	France	$1.41° \times 1.41°$	34	MIROC-ES2L	Japan	$2.81° \times 2.81°$
14	CNRM-CM6-1-HR	France	$0.5° \times 0.5°$	35	MPI-ESM1-2-HR	Germany	$0.94° \times 0.94°$
15	CNRM-ESM2-1	France	$1.41° \times 1.41°$	36	MPI-ESM1-2-LR	Germany	$1.88° \times 1.88°$
16	E3SM-1-1	USA	$1° \times 1°$	37	MRI-ESM2-0	Japan	$1.13° \times 1.13°$
17	EC-Earth3	Europe	$1.41° \times 0.35°$	38	NESM3	China	$1.88° \times 1.88°$
18	FGOALS-f3-L	China	$1.25° \times 1°$	39	NorESM2-LM	Norwegian	$2.5° \times 1.88°$
19	FGOALS-g3	China	$2° \times 2.25°$	40	NorESM2-MM	Norwegian	$1.25° \times 0.94°$
20	FIO-ESM-2-0	China	$1.25° \times 0.94°$	41	TaiESM1	Taiwan	$1.25° \times 0.94°$
21	GFDL-CM4	USA	$1.25° \times 1°$	42	UKESM1-0-LL	United Kingdom	$1.88° \times 1.25°$

3. Methodology: Quantile Calculation, Mapping

To accurately characterize the future climate-driven changes in environmental properties, it is not sufficient to estimate changes in average values alone. Information about the transformation of extreme event statistics is also crucial. However, a data-model comparison has shown that simulated extreme events are always underestimated, making direct calculations from model data unproductive.

Fortunately, this problem can be addressed effectively by using the fact (established in this study) that probability distribution functions are stable. It has been demonstrated that the same distribution laws apply to meteorological data observed in the YaNAO and the surrounding territories' stations. Specifically, average monthly temperature values are best approximated by a normal distribution, while precipitation is typically modeled using the Weibull distribution.

For example, monthly average precipitation (Pr) can be modeled using the Weibull cumulative distribution function (cdf):

$$F(Pr) = 1 - \exp\left(-A(Pr)^k\right). \quad (3)$$

This expression (stretched exponential distribution) can be replaced by

$$ln[-\ln(1-F)] = klnPr + lnA \quad (4)$$

Such representation allows a straight representation of the empirical function on the coordinate axis of the Weibull distribution. The model parameters (A and k) can be estimated using the maximum likelihood approach.

To assess the accuracy of the approximation, we traditionally calculate the coefficient of determination (R^2), which shows how well-observed outcomes are reproduced by the linear regression model and is the square of the sample correlation coefficient. In Figure 1, we plot 11 empirical "Weibull Plots", which are a specific nonlinear transformation of the data. Straight lines are recovered if the samples are Weibull. We can observe that the empirical cdfs at all sites do not consistently deviate from the theoretical lines, indicating that the Weibull distribution is a good approximation of precipitation. The scatter of lines and their different slopes reflect differences in precipitation patterns within the YaNAO.

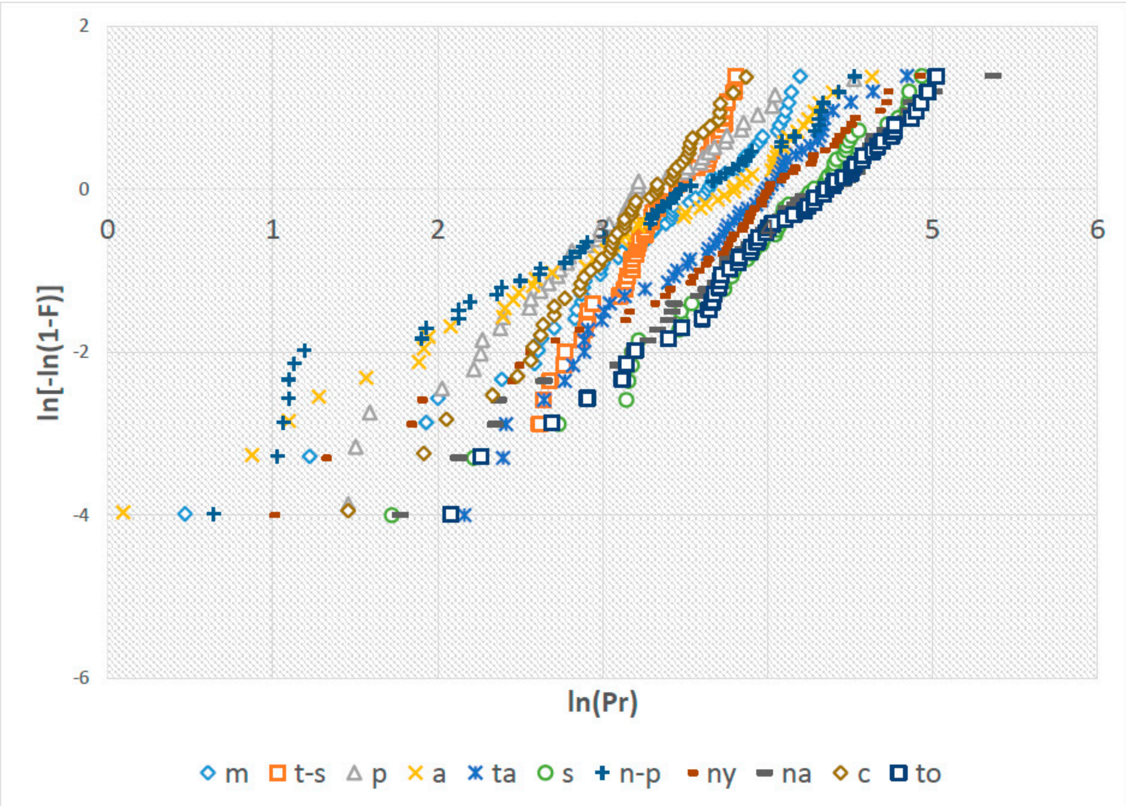

Figure 1. Empirical cumulative distribution functions of monthly averaged precipitation (station observations, July) straightening on the coordinate axis of the Weibull distribution. For any station, its distribution approximates the linear regression line corresponding to the Weibull function. In all cases $R^2 > 0.96$. m—Marresale, t-s—Tarko-Sale, p—Popova station, a—Antipayuta, ta—Tazovsk, s—Salekhard, n-p—Novy Port, ny—Nyda, na—Nadym, c—Chalasavei, to—Tolka.

In order to calculate the transformation of the function under climate change based on the hypothesis of preserving the function type, we need to compare the distribution parameters with statistical characteristics that are determined by the cumulative behavior of random variables in the sample. These include not only the mean value but also the standard deviation, median, and mode. The standard deviation is the mathematical expectation of the squared deviation of a random variable from its average value over the sample, with rare extremes playing minor roles. The median describes data compared to the mean and is not skewed by a small proportion of extremely large or small values, providing a representation of a "typical" value. The mode is the value that is most likely to be sampled.

Therefore, in the first stage, changes in the mean (μ), standard deviation (σ), mode (Mo), and median (Me) were estimated for January and July based on Formulas (1) and (2). The values are presented in Tables 3 and 4.

Table 3. Change of statistical characteristics of air temperature (°C) by the middle of the century for meteorological stations of the YaNAO.

Station	January				July			
	Mean	**Std**	**Mode**	**Median**	**Mean**	**Std**	**Mode**	**Median**
Popova station	4.56	0.54	3.56	4.83	2.45	0.44	1.53	2.56
Marresale	4.33	0.45	3.35	4.61	2.70	0.40	1.82	2.81
Antipayuta	3.61	0.39	3.33	3.76	2.59	0.29	1.91	2.73
Tazovsk	3.46	0.38	3.25	3.55	2.48	0.27	1.86	2.78
Salekhard	3.58	0.24	3.12	3.81	2.41	0.26	1.47	2.53
Novy Port	3.59	0.31	3.31	3.67	2.56	0.30	1.66	2.76
Nyda	3.51	0.28	3.21	3.74	2.52	0.32	1.47	2.81
Nadym	3.43	0.29	2.97	3.63	2.42	0.27	1.50	2.74
Tarko-Sale	3.34	0.39	2.87	3.33	2.39	0.27	1.63	2.57
Chalasavei	3.17	0.40	2.35	3.34	2.36	0.31	1.55	2.31
Tolka	3.14	0.38	2.65	2.30	2.41	0.28	1.67	2.37

Table 4. Change of statistical characteristics of monthly averaged precipitation amounts (mm) by the middle of the century for meteorological stations of the YaNAO.

Station	January				July			
	Mean	**Std**	**Mode**	**Median**	**Mean**	**Std**	**Mode**	**Median**
Popova station	3.90	0.22	3.11	4.90	1.95	0.03	0.19	3.36
Marresale	4.65	0.61	3.78	4.51	0.42	−0.47	−3.54	3.68
Antipayuta	4.02	0.40	2.54	4.82	0.44	0.08	0.86	-0.50
Tazovsk	4.27	0.69	2.02	4.65	1.39	−2.90	3.70	1.56
Salekhard	4.30	0.37	2.84	4.80	3.04	0.75	−1.30	2.47
Novy Port	4.34	0.78	1.47	5.37	0.38	0.15	−2.81	1.89
Nyda	4.28	0.80	2.20	4.82	−0.49	0.60	−5.59	1.16
Nadym	4.30	0.65	2.71	4.58	0.37	0.44	−6.66	0.84
Tarko-Sale	4.52	0.44	3.91	4.68	0.01	−0.88	−4.74	0.83
Chalasavei	4.68	0.48	4.76	3.54	0.32	0.29	−5.82	1.32
Tolka	4.68	0.28	4.27	4.69	−0.02	1.79	−7.73	−0.06

In the next stage, assuming the preservation of the Gaussian distribution for temperature variations, we can calculate quantile values using the following formula:

$$T_p = \mu + \sigma\sqrt{2}erf^{-1}(2p-1) \quad (5)$$

Here, erf denotes the Gauss error function, p = 0.95 or p = 0.05.

Since the Weibull distribution fits well with the precipitation data in all cases, it is possible, assuming the preservation of the distribution form, to determine the new parameters (k and A) from the solution of the system of two equations:

$$Mo = (Ak)^{-1/k}(k-1)^{1/k}$$
$$Me = (A)^{-1/k}(ln2)^{1/k}$$

The estimated parameters allow us to calculate the quantile function for the Weibull distribution as follows:

$$Pr(p) = \left(\frac{1}{A} ln \frac{1}{1-p}\right)^{1/k} \tag{6}$$

Here, $p = 0.95$.

Using the realized method, we were able to calculate quantiles that characterize monthly mean values. However, when empirical cdfs were calculated based on daily averaged amounts, they consistently deviated from the theoretical line for certain large threshold values. This suggests that the empirical tail diverges from the base model, indicating that different models may describe the data well. While such extreme events are rare, their presence has significant implications, as they represent the greatest extremes [8,9]. Nevertheless, when information is averaged monthly, the contribution of such exceptionally rare events is not felt.

The plain territory of the YaNAO, except for the western border part, as well as a fairly smooth change in prognostic values across the territory (see Tables 3 and 4), allows us to use information with a rather coarse resolution (on a $1^\circ \times 1^\circ$ degree grid). Note that the spatial resolution of climate models (see Table 2) does not allow for greater detail of information.

Prior to analysis, it is necessary to ensure that the quality of these data is appropriate for the objectives. For this purpose, the null hypothesis was tested. In investigating the null hypothesis that the sample mean m (averaged value around all climate models) is equal to a modern climate mean value μ, one uses the statistic $t = (m - \mu)/\left(s/\sqrt{n}\right)$, where s is the sample standard deviation and n is the sample size. The significance level for the study was chosen to be 5%. For the YaNAO territory, the intermodal standard deviation of temperature and precipitation variations is approximately 4–4.5 °C and 20 mm, respectively. For such values, the null hypothesis is true if each point of a $1^\circ \times 1^\circ$ degree grid is analyzed independently. However, for all $1^\circ \times 1^\circ$ arrays belonging to the YaNAO area, the null hypothesis can be rejected for predicted temperature and precipitation (besides the warm season's precipitation) in favor of the alternative hypothesis. Note that we did not use all ~400 grid points covering the YaNAO territory, but only about 100 sparse values, in order to refuse the dependence of the data.

Hence, the YaNAO area will be warmer in January by 3.5 °C (on the coast, even more by 4.5 degrees). Warming in July is around 2.5 °C everywhere (Table 3). Quantile values T (0.05) and T (0.95) increase by 3 and 4.5 °C in January and by 2 and 3 °C in July, consequently (Table 5). Hence, warming is expressed as a shift of both average and quantile values while the spatial features of the temperature picture are preserved.

Table 5. Quantile monthly averaged temperature values T (0.05) and T (0.95) in °C for data from measurement stations (1966–2018) and for data from climate simulations at the middle of the century.

Station	January		July	
	***T* (0.05)** at the Middle of the Century/Modern	***T* (0.95)** at the Middle of the Century/Modern	***T* (0.05)** at the Middle of the Century/Modern	***T* (0.95)** at the Middle of the Century/Modern
Popova station	−28/−31	−9/−15	3/2	11/8
Marresale	−26/−30	−8/−13	5/3	15/12
Antipayuta	−32/−35	−14/−19	9/7	19/16
Tazovsk	−32/−35	−14/−18	13/11	21/18
Salekhard	−28/−31	−13/−17	13/11	21/18
Novy Port	−29/−32	−12/−17	10/8	19/16
Nyda	−29/−32	−12/−16	13/11	21/17
Nadym	−29/−32	−11/−15	14/12	22/20
Tarko-Sale	−31/−34	−12/−16	15/13	23/20
Chalasavei	−30/−33	−11/−15	15/13	23/20
Tolka	−32/−34	−12/−16	15/13	23/20

Monthly averaged precipitation will increase by 10% in January, and they remain unchanged in July (Table 4), while quantile values Pr (0.95) increase by 30 and 10% in January and July, consequently (Table 6). A large increase in extreme precipitation during winter, together with warming, reflects that cyclone penetration from the west will become more frequent than under current conditions.

Table 6. Quantile monthly averaged precipitation values *Pr* (0.95) in mm for data from measurement stations (1966–2018) and for data from climate simulations at the middle of the century.

Station	January		July	
	Modern	At the Middle of the Century	Modern	At the Middle of the Century
Popova station	34	47	55	68
Marresale	35	45	64	76
Antipayuta	28	43	101	98
Tazovsk	63	77	95	91
Salekhard	35	49	133	146
Novy Port	37	58	91	100
Nyda	38	52	130	148
Nadym	40	57	154	173
Tarko-Sale	45	55	117	135
Chalasavei	45	46	126	146
Tolka	51	64	145	162

Having ownership of data on climate change, we can now move to analyze environmental changes. For the transition from climate variations to environmental changes, we use simple algorithms based on simple parameterizations that do not contain any non-stationary effects. As was shown, modeled data should be used for the whole area of such scale. Where necessary, these data are supplemented by specific properties of soils, permafrost, and vegetation, creating the mosaic of environmental response to global climate change (see below).

When using object-oriented models to project the impact of future climate change on studied processes or phenomena, it is important to provide justification for why and how the statistical relationships established in the present will still hold true in the future. The reliability of these relationships stems from their basis in physically-related processes. These models are tuned using modern observational data, which allows them to capture and represent the underlying mechanisms of the studied processes or phenomena. An alternative approach, in abstract terms, could involve coupling an Earth system model with a landscape schema. However, the complexity of the landscape schema far exceeds that of the surface schemas integrated into current Earth system models. The landscape schema would need to describe the thermodynamics and hydrodynamics of the soil under conditions of unsteady permafrost melting and account for the development of new forms of vegetation, which also influence heat exchange. Additionally, this approach would require information about climatogenic successions that are currently unavailable and numerous unknown parameters that would need to be considered. In contrast, the applied approach, which utilizes object-oriented models based on statistical relationships, is currently the most practical and capable of providing valuable results. These models, grounded in physically-related processes, capture the observed relationships between variables and can be tuned using available observational data. While they may not account for all the complexities of the landscape schema, they are still reliable for projecting the impact of future climate change on the studied processes or phenomena within their limitations.

The creation of cartographic representations is an important tool for predicting climate change and assessing its impact on the environment and climate-dependent sectors of the economy. We developed cartographic materials using traditional mapping methods and geoinformation technologies. The mathematical basis of the created maps, including the choice of a cartographic projection and the preparation of general geographic data, was developed. All layers in the shared geographic framework were integrated into the ArcGIS (ESRI) workspace. Next, all materials were digitized and integrated into the working area as separate data sets. Some of the resulting data were obtained in the modeling process based on the initial data.

4. Results and Discussion

4.1. Climate Change and Changes in the Frequency of Frosts and Thaws

The frequency of frosts and thaws varies with climate change depending on the air temperature regime. The algorithm used to study possible changes in the frequency of days with frosts/thaws in the middle of the 21st century on the territory of YaNAO at meteorological stations listed in Table 1 was as follows:

- A day with frost/thaws was considered a day when the air temperature was negative/positive in at least one observation hour and when the long-term average monthly temperature was positive/negative;
- Observation data was selected (1966–2018) at meteorological stations with a three-hour time resolution [Russian Research Institute for Hydrometeorological Information–World Data Center, http://meteo.ru, accessed on 1 January 2020];
- The frequency of frosts/thaws was calculated for each year at every station within the modern climate period (1966–2018), specifically for the months of June, July, August, and December, January, February. The aim was to investigate the statistical relationship between the mean seasonal and yearly air temperatures and the frequency of frost/thaw days. It was found that there is a significant linear relationship between frost/thaws. In this region, the warm period largely coincides with the summer months, while the cold period spans approximately 7–9 months. Therefore, the temperature during the cold period significantly influences the annual temperature. As a result, it was decided to use this data to establish a relationship with the frequency of thaws;
- Projected monthly mean air temperatures for the modern climate numerical experiments (2015–2025) and the middle of the century (2035–2065) were interpolated from a regular grid of 1×1 degrees of latitude and longitude to the location of every station;
- Statistical relationships for frost/thaws and mean temperature values were applied to the modern station data. The frequency of frosts/thaws was calculated;
- To project the frequency of frost/thaws in the middle of the 21st century, anomalies of their frequency were estimated.

At the stage of studying the current data, it was shown that there is a high correlation (-0.94) between the number of days with frosts and the average temperature for the period June-August (the plot is not presented). The equation of linear dependence is as follows: $y = -1.072x + 17.62$, where x is the average air temperature for the period June-August in degrees Celsius, and y is the number of days with frosts.

Using the known projected temperature, the number of days with frosts in the middle of the 21st century was calculated. Then, the difference between the values for the middle of the 21st century and the current climate was estimated. The results are presented in Figure 2.

As can be seen, the decrease in the number of days with frosts is most pronounced in the northern part of the YaNAO. In the north of the Yamal and Gydan peninsulas, by the middle of the 21st century, the frequency of frosts in June-August may decrease by 11 days. To the south, the values of anomalies decrease rather quickly, and in the south, they are one or two days.

With the onset of climate change, the frequency of thaws may increase. This change may be caused by alterations in the atmospheric circulation regime and a general rise in air temperature, especially in the Arctic and particularly in YaNAO. During the current climate study, a high correlation (-0.98) between the average annual temperature and the number of days with thaws was found (the plot is not presented). The linear equation for the relationship is $y = 4.7x - 1226.1$, where x is the average annual air temperature in degrees Kelvin, and y is the number of days with frosts. Using this equation, the number of days with thaws was calculated for future climate scenarios, and the difference between the projected values and the current climate was determined. Calculations indicate that the increase in the number of days with thaws during the cold season is minimal and least pronounced in the northern part of YaNAO, namely in the north of the Yamal and Gydan Peninsulas. To the south, anomalies values are between 0.2–0.3 days. The small average multiyear deviation value may be related to the fact that the air temperature usually remains negative from October to April, when the climate warms up, and the frequency of thaws increases insignificantly.

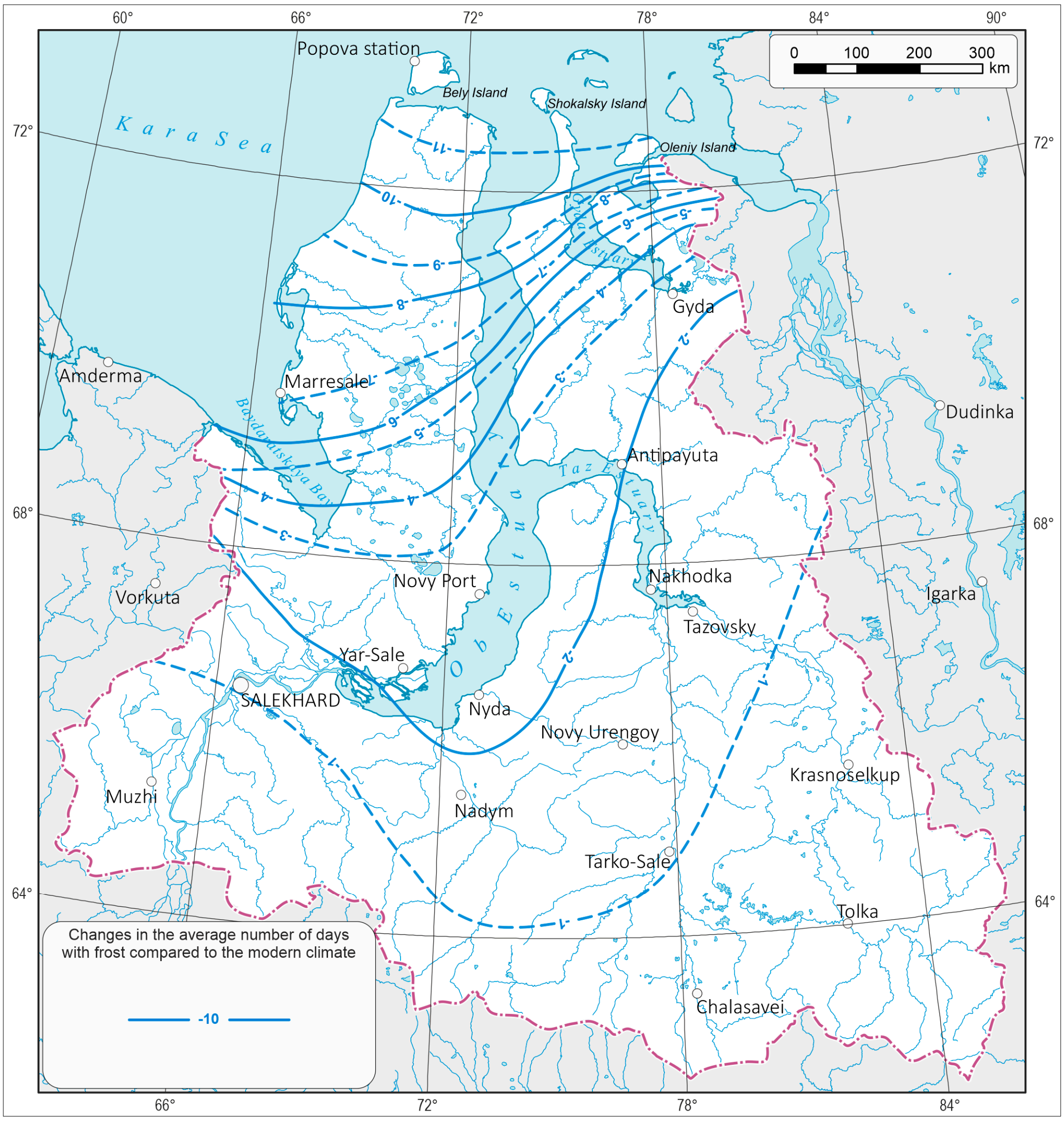

Figure 2. Anomalies in the average number of days with frost in the mid21st century for June-July-August compared to modern climate.

Therefore, the strong statistical relationship between air temperature and the number of frosts in the warm season and thaws in the cold season in the current climate allowed for the projection of these indicators for the middle of the 21st century. The obtained results demonstrate that Arctic amplification, i.e., a significant increase in projected temperatures in the Arctic, has a more significant effect on the decrease of frosts in the warm season than on the number of thaws. As winter temperatures remain strongly negative in the middle of the century, the number of thaws changes insignificantly.

4.2. Climate Change and Changes in the Avalanche Parameters

The influence of climate change on avalanche activity is being studied in different countries. For example, in the French Alps and Switzerland, there has been no significant increase in avalanche frequency since 1950 [22,23]. However, in the Italian Alps, there has been an increase in avalanche activity since 1980 [24]. In this paper, we will attract attention to the polar region.

In the YaNAO, avalanche-prone areas are located in the eastern part of the Polar Urals and the mountain ranges at the northern tip of the Ural Range. This area is characterized by a long period of avalanche hazard lasting 200–220 days, associated with a cold winter, sufficient solid precipitation, and frequent strong winds and snowstorms.

The relief determines the formation of both flume and slope avalanches. Snowstorms are the main factor in avalanche formation in winter. In the current climate, the frequency of snowstorms is 150 days per year. In the axial parts of the range, about 2–3 avalanches occur per year (volume is 10,000–100,000 m^3). On the eastern slope of the Ural Mountains, an equal volume of snow avalanches less often (0.5–1 avalanche per year).

The methodology of small-scale mapping of avalanche activity characteristics for poorly studied mountain regions of the Former USSR [25] was used to study the dynamics of avalanche activity characteristics due to climate change. Data collected in well-studied avalanche areas allow us to establish a connection between avalanche activity indicators and general factors of avalanche formation, which could also be valid for unstudied territories or to predict future situations. Methods were developed for determining avalanche activity indicators from climate characteristics, which were collected at more than 700 meteorological stations in Russia [25]. The correlation coefficient of data on individual weather stations and the compiled dependency curves is at least 0.8–0.9. Based on these relationships, we determined the average values of the maximum ten-day snow cover thickness (Hm), the duration of the avalanche period (Davp), and the frequency of avalanches for the grid nodes of the considered climatic model.

It has been established that the average long-term frequency of avalanches Nav in avalanche catchments of medium activity depends on the average long-term value of the maximum decade snow cover depth Hm. Hm is determined using the dependence on Px-the amount of precipitation in the cold period (November-March) and T_I, which is the average temperature of the coldest month (January for the Polar Urals). It was found that an increase in the height of snow cover in the Polar Urals is expected by the middle of the 21st century, and only at the southeastern tip of the range are no changes expected.

The dependence of Nav on Hm and T_I was determined and presented in Table 7. This indicator would triple if we counted all avalanches, even the smallest ones. Based on the values of Hm, we obtained the calculated frequency of avalanches, which increases along the entire ridge by 10%, and in the axial parts of the Polar Urals by 20%.

Table 7. Dependence of the average long-term frequency of avalanches reaching the valley floor, on average for avalanche activity N_{av}, on the average long-term value of the maximum decade snow depth H_m [25].

N_{av}	H_m for Areas with Mean Temperature of the Coldest Month, cm	
	Below −20 °C	Above −20 °C
less than 1	40–70	30–50
1–10	70–120	50–100
over 10	over 120	over 100

One of the most important indicators of future avalanche danger is the Davp. Based on the obtained values of Ns and the already known Hm using the established dependencies, we calculated the Davp by 2050. It is expected that in most of the Polar Urals, the duration of the avalanche period will not change over the winter and will remain within the current values. However, in the axial parts and the northern part, Davp will increase by 5–10%.

As a result of our calculations, we predict that despite the increase in temperature, there will be a significant increase in the level of avalanche danger in the Polar Urals in the YaNAO by 2050 compared to the current period. This will happen due to an increase in the amount of solid precipitation in winter, leading to an increase in the thickness of the snow cover and an increase in the frequency of avalanches in almost all of the study area. In addition, there will also be an increase in the duration of the avalanche period in some areas.

4.3. Debris and Slush Flows under Climate Change

Debris flow is a rapid to extremely rapid flow of saturated non-plastic debris in a steep channel [26]. In the YaNAO, debris flow processes are active in the Polar Urals, over a 400 km long area from northeast to southwest, with a width of about 50 km. The main type of debris flow here is a slush flow, which is a flowing mixture of water and snow [27]. Slush flows are widely distributed within the axial zone of the Polar Urals, where snow accumulation is highest. Areas of potential debris flow hazard are identified by topographical indicators, such as relative mountain height and slope angles, taking into account data on mudflows observed historically. Slush flows are numerous and typically form in May–June. The main condition for their formation is a sharp rise in average daily air temperature by 7–10 °C within 2–3 days. The frequency of slush flow occurrence, according to limited data for the Polar Urals, is every 7–10 years [11]. In July–August, rare rain mudflows occur, mostly as small slope debris flows.

The characteristic volume of material transported by slush flows is tens of thousands of cubic meters, with the largest deposits recorded in May 1973 in the basin of the Bolshaya Paipudyna River (a tributary of the Sob River, on the western slope of the Polar Urals), which amounted to 500,000 cubic meters. This is the maximum value for the snow-type of mudflows in Russia [11].

The spatial distribution of hazardous areas for slush flows is determined mostly by topography and will not change by 2050, in contrast to their frequency and intensity. Slush flows depend on two major climatic factors: winter snow accumulation and spring air temperatures. It is possible to assess the growth of slush flow hazard in YaNAO by 2050, taking into account the following predicted changes in climatic parameters: (a) an increase in winter precipitation by 10–15%, (b) an increase in spring air temperature by about 3 °C, (c) an increase in the standard deviation of air temperature values (up to 0.4 °C).

Regional variability of slush flow hazard can only be assessed in general terms since, at this modeling scale ($1^\circ \times 1^\circ$ grid), only six grid nodes fall within the debris flow hazardous area. Snow accumulation will increase somewhat more in the northern part of the slush flow development area, especially on the western slope of the Polar Urals. The increase in liquid precipitation here will be up to 22 mm of water equivalent (w.e.) for November–March. A slightly smaller increase will be observed in the south of the region and on the eastern slope (an increase of 18–19 mm w.e. for November–March). The occurrence of sharp warming events, which are one of the main reasons for slush flows, can be indirectly inferred from the variability of air temperature in spring. By May 2050, the standard deviation of air temperature will increase by 0.3 °C (almost uniformly within the region), and in June by 0.3–0.4 °C, with a more pronounced increase in the south of the area (in contrast to the greater increase in snow accumulation in the north).

Thus, slush flow hazard will grow evenly within the mudflow-prone area by 2050. The main recommended protection measures are those aimed at preventing and ensuring the safe placement of facilities based on a thorough assessment of the territory. Additionally, liquid runoff can be regulated by creating reservoirs, upland canals, and other measures.

4.4. Climate Change and Changes in the Retrogressive Thaw Slumps

Landslides are a type of dangerous slope process. A distinctive feature of the landslide mechanism is the rocks sliding down the slope. The landslide processes are always hydrogeologically determined. They occur when water-permeable rocks are underlain by a layer of water-resistant rocks. A specific geological structure can favor the formation of landslides when the inclination of the water-resistant rocks' roof coincides with the surface slope. This is most often observed within the permafrost zone when seasonal thawing occurs on slopes. In areas outside the permafrost zone, landslides typically occur on slopes of 15° or more, while in the permafrost zone, a slope of 4–6° is sufficient for the development of landslides [12].

Within the YaNAO, landslide processes are mainly represented by retrogressive thaw slumps (RTSs). In this case, the aquifer is the roof of permafrost under the seasonally thawed (active) layer. RTSs are among the most active relief-forming processes in the Arctic; their number has increased significantly in recent decades [12]. Since the beginning of the 21st century, the RTSs have become more numerous across the ice-rich morainal landscapes of the western Canadian Arctic [28,29]. The observed climatic changes and the subsequent increase in the depth of seasonal thawing in the long term can lead to the activation of cryogenic landsliding. On Banks Island, Canada, between 1984 and 2015, 4000 new RTSs emerged, primarily following four particularly warm summers [28]. At the same time, in the short term, the activity of RTSs depends not only on climatic factors but also on the ground ice distribution parameters [29].

Two types of cryogenic landslides are distinguished. Translational landslides (active-layer detachments) are the result of the displacement of blocks of the thawed part of the active layer along a frozen icy base. RTSs (or cryogenic flows) are a consequence of the loss of stability of water-saturated soils in the active layer, which causes a mud flow along the surface of ice or icy sediments. Each type of cryogenic landslide has distinctive morphological features. Active-layer detachments typically have an intact landslide body with ledges at its boundaries, while RTSs have a disintegrated landslide body and form thermocirques. RTSs are common in areas with massive ice or icy sediments, as their distribution is geologically predetermined.

RTSs are activated by an increase in summer air temperature, which causes ground ice to melt more quickly. However, this process also contributes to the accumulation of landslide deposits and can lead to the attenuation of the RTS until the next heat influx. It should be taken into account that RTSs depend not only on interannual climatic fluctuations (because thermocirques in different phases of development, both new and stabilizing, occur simultaneously on the same territory) but also on geological, geomorphological, and random factors.

To assess the risk of RTS activation by 2050, we considered their current distribution, as their recurrence in thermocirques span decades. The activation of active-layer detachments depends on a more complex set of conditions, and the cycle length is centuries.

RTS leads to the formation of a specific thermal denudation landform—the thermocirque—which is well identified both in the field and on high-resolution satellite images. An inventory of thermal cirques in the north of Western Siberia was recently carried out based on a mosaic of high-resolution satellite images from 2016–2018 [30], and active and stabilized thermocirques were identified. Based on this inventory, three types of areas were distinguished within the YaNAO according to their RTS activity: (1) areas with numerous RTSs, (2) areas with single RTSs, and (3) areas where RTSs are almost absent.

Of the climatic parameters influencing cryogenic landslides, we considered precipitation and summer temperatures. The amount of precipitation (both winter and spring–summer) determines the moisture content in the active layer soils. We analyzed the increase in precipitation (in mm w.e.) by month in areas where RTSs are numerous. The maximum increase in precipitation (approx. +7 mm w.e. per month) is predicted in October–November in northeastern Gydan.

To take into account the temperature factor, we analyzed the increase in summer temperatures by 2050. A uniform increase in average monthly temperatures is predicted throughout the area of RTS distribution (about 2 °C) from June to September. Since the activation of RTSs depends not only on the absolute values of temperature growth but also on the variability of temperatures between the coming years, we considered the standard deviation of August air temperatures (the warmest month) in the YaNAO. Within the area of RTS development, the maximum increase in the standard deviation of August temperatures (up to 0.3 °C) is predicted in the northeast of the Gydan Peninsula, with background values of the increase in the standard deviation of 0.2 °C.

Based on data on the distribution density of thermocirques and the results of climate forecasts, we identified areas of higher risk of RTS activation in the middle of the 21st century (Figure 3). These include areas in Western Yamal and a 100 km strip in the north of Gydan, which includes the Gydan Ridge and territories to the north of it. Areas of higher risk of RTS development in the middle of the 21st century generally coincide with the areas where RTSs are numerous today. Only in the northeast of Gydan are the high-risk areas somewhat expanded. Here, a greater increase in precipitation is predicted, as well as somewhat greater temperature variability (the probability of the emergence of new thermocirques increases with large interannual fluctuations in summer temperatures). Despite high ice content in the northern areas of Yamal and Gydan, there were no landslides found in these areas [30]. This can be connected with permafrost structure (predominance of marine Late Quaternary sediments) or lower depth of the active layer. So far, we do not predict their appearance by 2050.

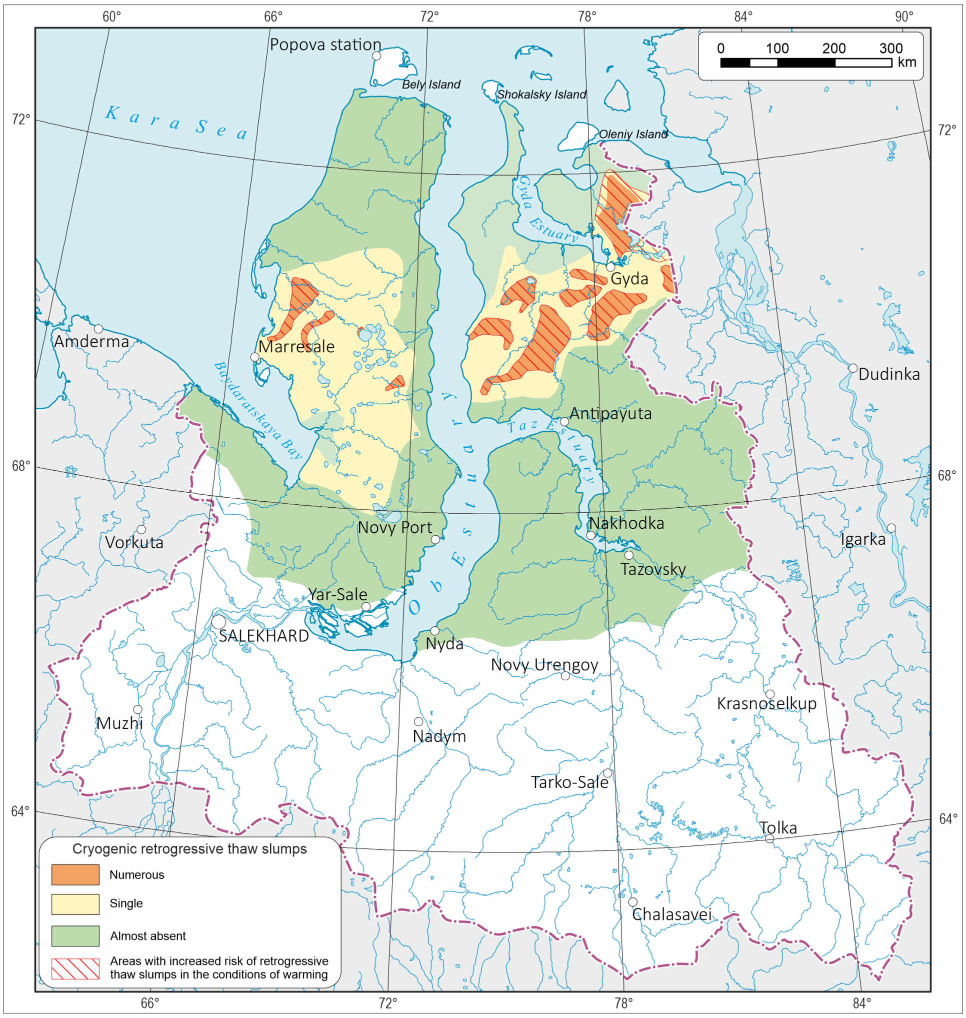

Figure 3. Retrogressive thaw slumps distribution and areas of their potential intensification by 2050. RTS distribution was drawn based on the identification made for 2016–2018 and massive ice beds' distribution [30].

Areas with single thermocirques are medium-risk areas associated with RTSs. The zone in which thermocirques are almost absent is bounded from the south by an area of continuous permafrost distribution; in this southern zone, the risks of RTS activation are minimal.

4.5. Climate Change and Changes in the Abrasion and Thermal Abrasion of the Kara Sea Coasts

According to its definition, abrasion is a process of mechanical destruction of coastlines and underwater slopes by waves, as well as the impact of water-borne detrital material. In the permafrost zone, in addition to mechanical abrasion developing under the action of waves, thermal or thermomechanical abrasion is also distinguished, which develops under the combined influence of wave and thermal factors.

Thermal abrasion is the destruction of the coast and the underwater slope composed of ice-bound permafrost sediments. It is a natural process that can become hazardous if it leads to serious complications in the conditions for nature management and development of the coastal zone. It consists of two processes: mechanical destruction of the coast and the underwater slope by waves, and thermal denudation, which is the thawing of frozen sediments of the coastal ledge under the action of water and air with positive temperatures [31]. The intensity of mechanical destruction is affected by the wave fetch and the duration of the ice-free period, which depend on the distribution of sea ice in the Arctic [32]. The intensity of thermal denudation is affected by the sum of positive annual air temperatures [33].

To identify future changes in the rates of thermal abrasion, the retreat rates of the thermoabrasional coasts of the Kara Sea over the past decades were analyzed. This analysis included field observation data, such as tacheometric measurements of coastal retreat of key areas. To ensure wide coverage, space images from the 1960s were also analyzed, and the position of the coastline was compared with modern images. These satellite images [https://www.usgs.gov/media/images/declassified-satellite-imagery-1-corona-table, accessed on 1 January 2020], which have a spatial resolution of up to 2 m, were purchased in advance and were available for most of the territory. They were processed and spatially referenced, and the position of the coastline at the date of image acquisition was determined. For thermoabrasional segments, the edge of the cliff was traced according to the methodology previously used and described in [34–36]. In the final stage, the position of the coastline in the past was compared with the current position obtained from modern satellite images. This approach revealed the modern mean annual rates of the coastal retreat. To verify the obtained rates, the published data on the rates of coastal retreat in key areas were used. Based on the obtained average long-term erosion rates, a map for the modern conditions was created. In accordance with the calculated rates of coastal retreat, the segments were divided into categories based on the degree of risk: non-hazardous (accumulative or stable coasts), moderately hazardous (average thermal abrasion rate from 0 to 0.5 m/year), hazardous (average thermal abrasion rate from 0.5 to 2 m/year), and very hazardous (average thermal abrasion rate of more than 2 m/year).

In the second stage, calculations were made of the interannual variability of the main parameters affecting coastal retreat–temperature and wind wave energy for key sites of coastal dynamics monitoring, where long-term measurements of coastal retreat rates with good time resolution had been carried out. The morphological and morphometric parameters of the coasts and their types were analyzed. The results of the comparison of archival satellite images of Corona with modern ones were used to determine the extent to which the morphological type of a given segment of the coast corresponds to its modern dynamics. Coastal morphology was analyzed using topographic maps, satellite images, and data from field studies. The morphology of the coast and its type (thermoabrasional, thermodenudational, accumulative, etc.) provide insight into its origin and the main processes that formed the appearance of the coast.

In the third and final stage, the obtained results were extrapolated to the entire territory, and a forecast was made for the rates of the thermal abrasion process by 2050. This forecast took into account the change in air temperature in the summer months. Those areas with access to the open Kara Sea are most susceptible to thermal abrasion; thermal abrasion is also developed on the banks of the Gulf of Ob.

At present, the coasts of the Kara Sea, located in the north of the YaNAO, recede at the highest rates, like the coasts of Bely Island, with average annual rates of up to 4 m/year [37]. In addition, the coasts in Western Yamal and within the Baydaratskaya Bay will quickly erode [38–40], especially where massive ice is exposed in the coastal bluff: on the southwestern coast of the Baydaratskaya Bay [34], near the Marresale weather station [38], Kharasavey settlement [39]. The rates of thermal abrasion in these areas will exceed 2 m/year, which allows them to be classified as very dangerous according to the classification of risks associated with thermal abrasion. Significantly lower rates of thermal abrasion will be observed on the shores of the closed water area of the Ob, Taz, and Gydan bays. However, there are also areas where the average annual rates of thermal abrasion will be from 0.5 to 2 m/year [41], which can be dangerous for coastal infrastructure.

To assess the impact of changing hydrometeorological parameters on thermal abrasion rates by 2050, it is crucial to identify the primary factors that influence this process. The most critical factor is the air temperature during the summer months, particularly in July, August, and September, when the sea is ice-free, and the air temperature is positive [33]. According to our results, it is expected that the increase in air temperature during these months will be up to 2 °C compared to current levels. This rise in temperature will lead to a higher rate of thawing of frozen soil in coastal bluffs, resulting in increased rates of thermal abrasion. Although the temperature increase will be uniform across the territory, its impact on the coasts will vary. The thermoabrasional coasts composed of icy sediments or deposits containing massive ice, such as the southwestern coast of Baydaratskaya Bay, Marresale, and Kharasavey, will retreat at the highest rates [32–34,42]. The coasts classified as very dangerous will expand, and new high-risk segments will emerge, such as the area south of Kharasavey, which is currently not dangerous [42].

Presently, the retreat rates of the thermoabrasional coasts of the Baydaratskaya Bay are less than 2 m/year, but outcrops of massive ice are observed in the coastal bluffs. With a further increase in air temperature, these outcrops will grow even more actively, and by 2050, the level of risk associated with thermal abrasion for some of the coasts will be classified as very dangerous.

The indirect effect of warming, in addition to the direct effect on permafrost thawing in coastal bluffs, will be even stronger. It will be manifested in the reduction of sea ice extent, which will result in an increase in wave fetch and a longer ice-free period. Northernmost coasts, such as the coasts of Bely Island and Shokalsky Island, will be most affected, and by 2050, they will retreat even faster, leading to the emergence of new areas belonging to the very dangerous category. Additionally, some of the coasts that were previously classified as accumulative by their morphology will begin to erode and move into the thermoabrasional category.

Low thermoabrasional coasts are particularly vulnerable as they require significantly less wave energy to move far inland and cause significant destruction. They will be able to retreat several meters or tens of meters during one storm or high surge event. These coasts are also under greater threat due to the ongoing sea level rise, which may have some impact on the retreat of thermoabrasional coasts of the Kara Sea by 2050, although not as significant as the temperature increase and increased waves.

4.6. Climate Change and Changes in the Suffusion (Internal Erosion)

Suffusion is an internal erosion process that occurs when finer soil particles detach due to seepage flow and start moving within the pore space of larger particles [43,44]. Geomorphologically, suffusion is involved in the formation of various subsidence landforms. The main favorable factors for the development of internal erosion are the presence of sands with the finest constituting particles, as well as highly dissected terrain, which contributes to increased filtration rates.

Internal erosion is a phenomenon that has not been studied enough [44,45]. Internal erosion has been noted in Salekhard city and near the coast in the Marresale weather station in the YaNAO, and an estimation of suffusion risk was made for the Sabetta area (eastern coast of Yamal Peninsula). Additionally, suffusion has been observed in coastal ledges. Technogenic sand is often used for the construction of foundations and basements in the YaNAO, which are subject to such processes. Due to ignoring surface runoff, lack of drainage, and disregard for topographic features, internal erosion can only intensify with climate change.

Data on lithology composition and the dissection of relief, including surface slopes, were analyzed [46,47]. Since heterogeneous grain-size composition sand is favorable for the development of internal erosion [48], the boundaries of the distribution of these soil types were outlined on the map. The silty fraction is widespread in soils of this region, and sands are no exception. Finer soil particles are detached, and removal from the stratum begins only with certain values of water pressure. Therefore, another factor is a dissected relief and/or the presence of a surface slope. Thus, the current state and risks associated with internal erosion were assessed by comparing areas with favorable factors and literature data. The analysis focused on studying the impact of climate change on suffusion by comparing spatial data on precipitation (separately for winter and summer) and air temperature. It was found that higher levels of precipitation favor the development of suffusion. The contours of precipitation during the warm and cold periods were identified, enabling the division of the study area based on current and projected precipitation levels for both the present day and 2050.

Maps of the average monthly air temperature for 2050 and maps of the difference between the average monthly air temperatures of today and 2050 were used. As a result, areas with different risks of suffusion development by 2050 were identified. An analysis of the internal erosion process for the Sabetta area [49] showed that about 25% of the territory has a high risk of suffusion development. However, this does not mean that 25% of the material will be removed from the soil layer. In permafrost, suffusion processes are local, and the size of internal erosion forms is a few meters. The volume of exposed rock deformation rarely exceeds 1 m^3/year.

Internal erosion processes develop to varying degrees throughout YaNAO (Figure 4). In areas with continuous permafrost (Yamal, Tazovskiy, Gydan peninsulas), the risks of suffusion processes under climate change are mainly local, occurring only within the seasonally thawed layer in the sides of ravines and on coastal slopes of seas, lakes, and rivers. The risks of suffusion processes in sandy soils will be greater than in loams due to their easier erodibility and lower natural moisture content, requiring less energy for the phase transition from frozen to thawed state. With climate change and an increase in air temperature and precipitation by 2050, sandy soils will thaw more intensively than loamy soils, with the greatest risks of suffusion in sands and the least in loamy soils and peats, which have high ice content.

In central and southern YaNAO, flat topography and swampy areas make internal erosion processes unlikely under climate change, except in areas with sandy and sandy loamy rocks that are subject to erosion with increased precipitation. In the western part of YaNAO, areas with sandy soils and a dissected relief will favorably affect the development of suffusion, increasing its risks under climate change. Areas with peat soils have low risks of suffusion due to their high ice content, which reacts inertly to climate change.

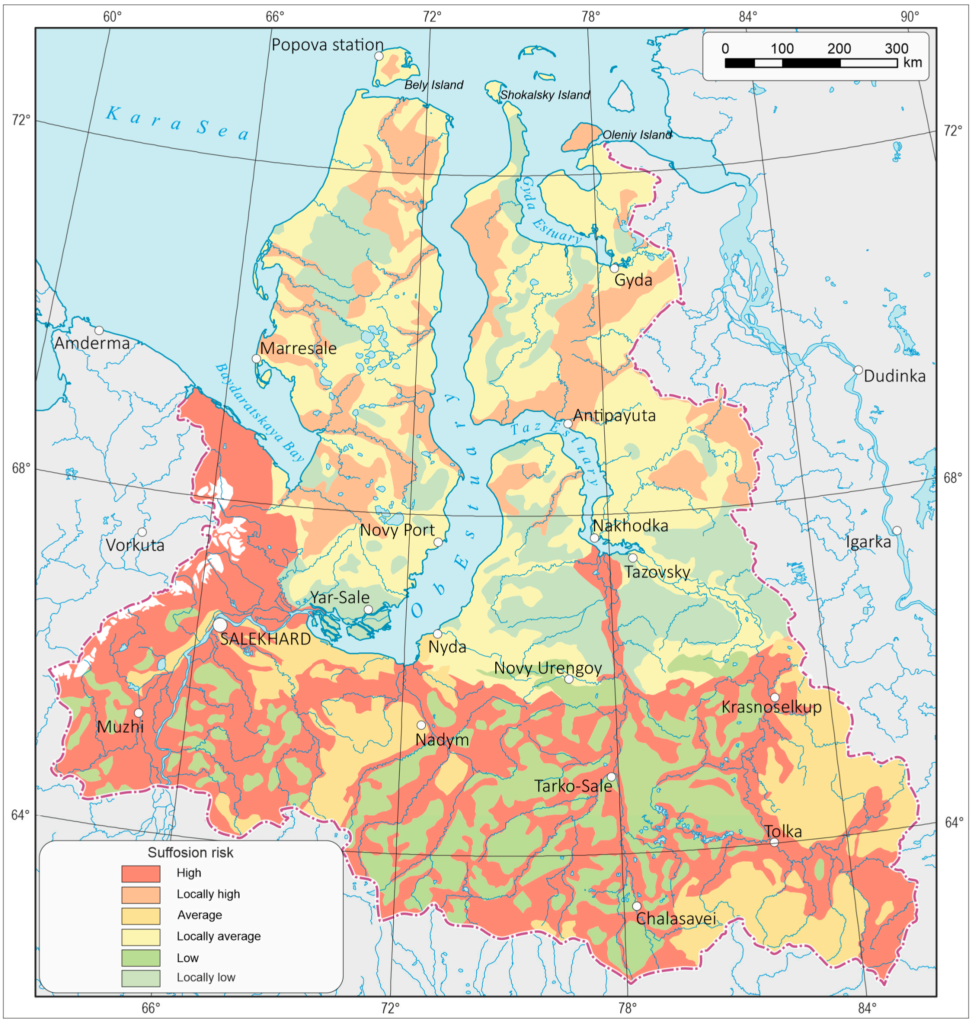

Figure 4. Intensity of internal erosion in YaNAO by 2050: high risk—a combination of more favorable factors for suffusion; average risk—some of the suffusion factors are positive, but not all; low risk—unfavorable factors for suffusion are prevailing. For continuous permafrost zones, suffusion will be local.

4.7. Climate Change and Changes in the Erosion Processes

Erosion processes refer to the various denudation processes related to water flow. Gully erosion, which is a linear mechanical destruction and removal of the products of this destruction, is one of the most dangerous land damage processes [50,51]. In riverbeds, deep and lateral erosion usually occurs. In permafrost conditions, the most hazardous process is thermal erosion, which is the destruction of unconsolidated frozen soils and ice wedges due to the thermal and mechanical effects of water flows. Thermal erosion is widespread in the YaNAO territory and has been described in detail in Yamal, especially in the areas of economic development [50,52]. Fine sands are most easily eroded [53], both in the thawed and frozen states, while loams and clays are eroded less.

Climate warming in YaNAO will affect erosion process activity through increased precipitation, air temperature, and, consequently, a rise in the depth of seasonal thawing. The rise of the active layer can lead to ice-wedge degradation and catastrophic thermal erosion development.

To identify areas susceptible to erosion processes, we analyzed data on lithology composition, ice content, relief dissection, and surface slopes [47]. In the subsequent stage, we mapped the areas where ice wedges are forming using modern satellite images, which allowed us to estimate the extent of current erosion activity. The obtained data from the analysis of these images were then compared with maps depicting the geological structure and ice content of rocks, relief dissection, and surface slopes. This comparison helped clarify the boundaries of regions with varying levels of erosion risk. To predict the development of erosion processes due to climate change, we considered current and projected data on air temperature (at the end of the warm period) and precipitation (for the winter period and at the end of the summer period). Higher levels of precipitation and elevated summer air temperatures are favorable for erosion development. Contour lines representing precipitation and air temperature regimes during the summer were identified. These contours were used to supplement the boundaries of regions with different intensities of erosion process risks, considering varying precipitation levels and air temperatures at the end of the warm period. Additionally, working with remote sensing data allowed us to analyze river valley sections and the characteristics of river channels. Riverbeds typically experience deep and lateral erosion. Due to sea level rise, the erosion base will also increase, leading to a higher occurrence of lateral erosion in the channels compared to bottom erosion. However, increased lateral erosion in rivers can further contribute to slope erosion by disrupting the equilibrium profile. As a result, areas with low rates of channel erosion may coexist with high-risk areas, exacerbating the erosion processes.

Currently, erosion processes occur throughout the YaNAO territory but with varying intensity (Figure 5). In Yamal, Gydan, and Tazovskiy peninsulas with continuous permafrost and a high dissection of the surface topography, ravine thermal erosion and high-intensity erosion predominate due to the wide distribution of ice wedges, which melting provokes the rapid growth of ravines. The activity of the gully process increases significantly in the paragenesis with river (coastal) erosion in the valleys. In addition, thermal erosion is widely developed on coastal cliffs.

Climate change, accompanied by an increase in air temperature during the warm period and an increase in precipitation (both in winter and summer), will only further contribute to the development of erosion processes. Therefore, these areas are shown on the map as highly intense. An important factor in the development of erosion processes is the technogenic impact. The main condition for the emergence and development of gully erosion is the complete or partial removal of the soil and vegetation layer, especially in linear form. On slopes, this leads to the interception and concentration of dispersed runoff during snowmelt and rainfall. The temporary eroding flows have a severe impact on frozen soils, especially sand, and the depth of incision can reach 8–10 m in just a few hours. As a result of deep erosion incisions, adjacent areas lose their stability at a distance exceeding the depth of the incision by 3–4 times. Such an incision, which is 100–300 m long, can turn into typical V-shaped ravines within a month [54]. Thus, climate change, together with the technogenic factor, can have catastrophic consequences for the territory as a result of the development of thermal erosion processes.

The southern and southeast parts of the YaNAO territory are located in the area of discontinuous permafrost, so climate change will not have such a strong effect on thermal erosion processes. However, since erosion gullies are one of the mechanisms of drainage of thermokarst lakes [52], and thermal erosion destruction of the bridge between the lake and the river can lead to a catastrophic (in 1–2 seasons) descent of the lake, these areas were highlighted on the map as having a medium intensity of development of thermal erosion processes.

Analysis of satellite images showed that all rivers in the YaNAO have a meandering channel. This type of channel indicates that lateral erosion with redeposition of alluvium predominates, and local deepening is weakened. Large rivers in some places have a branched channel, which indicates that accumulation in such parts prevails over erosion. Climate change, accompanied by an increase in precipitation and sea level rise, will contribute to further accumulation of material and slow down erosion activity in river valleys and flat areas. Accordingly, these areas on the map were marked as areas with the lowest intensity.

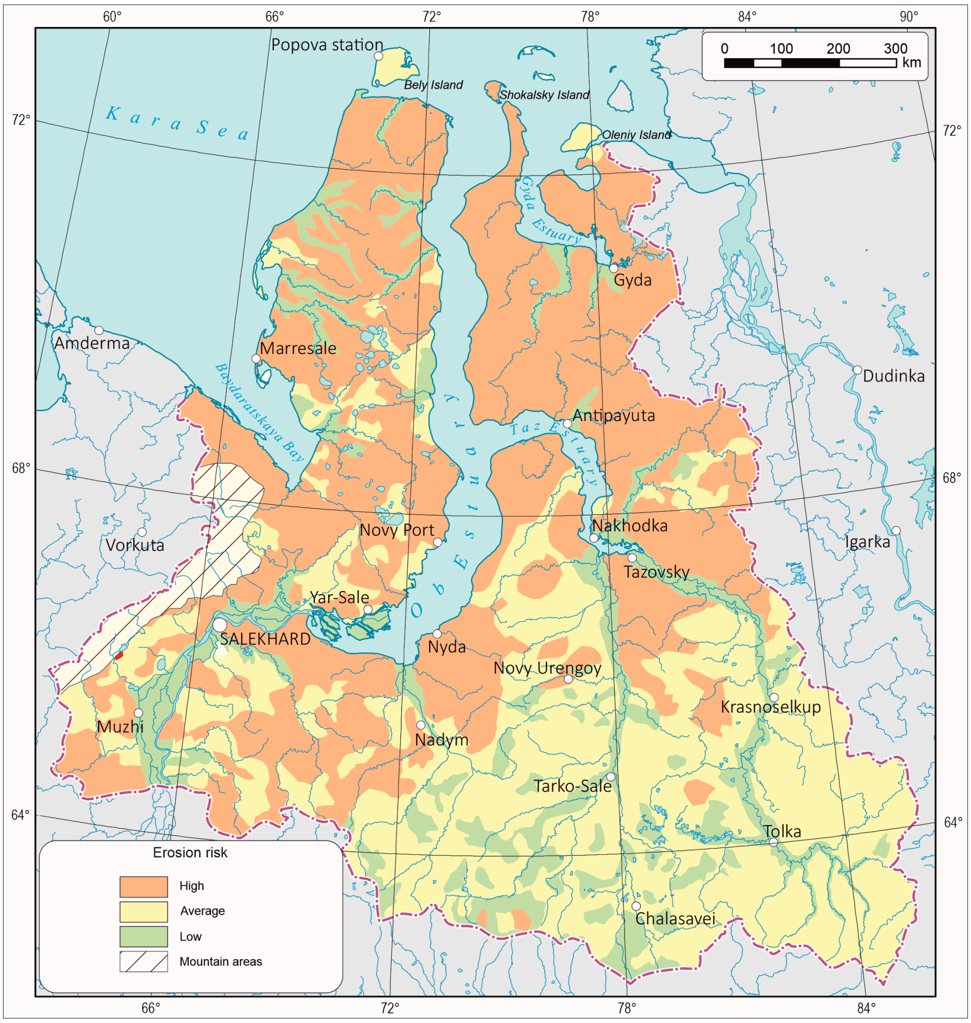

Figure 5. Intensity of erosion processes in YaNAO by 2050: high risk—combination of more favorable factors for erosion processes; average risk—some factors of erosion processes are positive, but not all; low risk—unfavorable factors for erosion processes are prevailing.

4.8. Climate Change and Changes in the Thermokarst

Thermokarst refers to a process whereby ice-rich deposits or ground ice thaws, causing the ground surface to subside and resulting in the formation of thaw depressions and lakes [19]. More than 40% of the permafrost region has been affected by thermokarst subsidence since the Little Ice Age, and new thermokarst terrain is currently forming. In Arctic Alaska, thermokarst rates increased by about 60% from 1950 to 2015 due to the warming climate. Similarly, climate warming in the YaNAO will affect thermokarst activity by increasing the depth of seasonal thawing in ice-rich soils, which will lead to subsidence and the formation of depressions where water can accumulate and further promote thermokarst development. To estimate the risks of thermokarst development, information concerning ice content in sediment at the upper part of the permafrost section is necessary.

To identify thermokarst, we analyzed data on lithology composition, ice content, and relief dissection, including surface slopes [47]. We excluded the contours of unfrozen soil and mapped the areas of current thermokarst development based on modern satellite images. To estimate the role of climate change, we analyzed data on air temperature during the warm season (June–September) and compared the contours of current thermokarst areas with maps of changes in average monthly air temperature. Finally, we compared maps of factors causing thermokarst development to identify areas with different risks of thermokarst during climate change.

Thermokarst is widespread in the YaNAO [52], particularly in the northern part, where continuous permafrost and ice-rich soils are found. An increase in air temperature and precipitation will increase the risks of thermokarst in these areas. Yamal has experienced a reduction in the number of large lakes and an increase in the number of small ones due to thermokarst, and these small thermokarst depressions pose different risks depending on the ice content. Areas with ice-rich loams are classified as very high risk, areas with icy loams and silts as high risk, and those with sand in the section as medium to low risk. In the southern and southeast parts of the YaNAO, many thermokarst lakes have already formed, which is why these areas are also characterized by very high risks on the map (Figure 6).

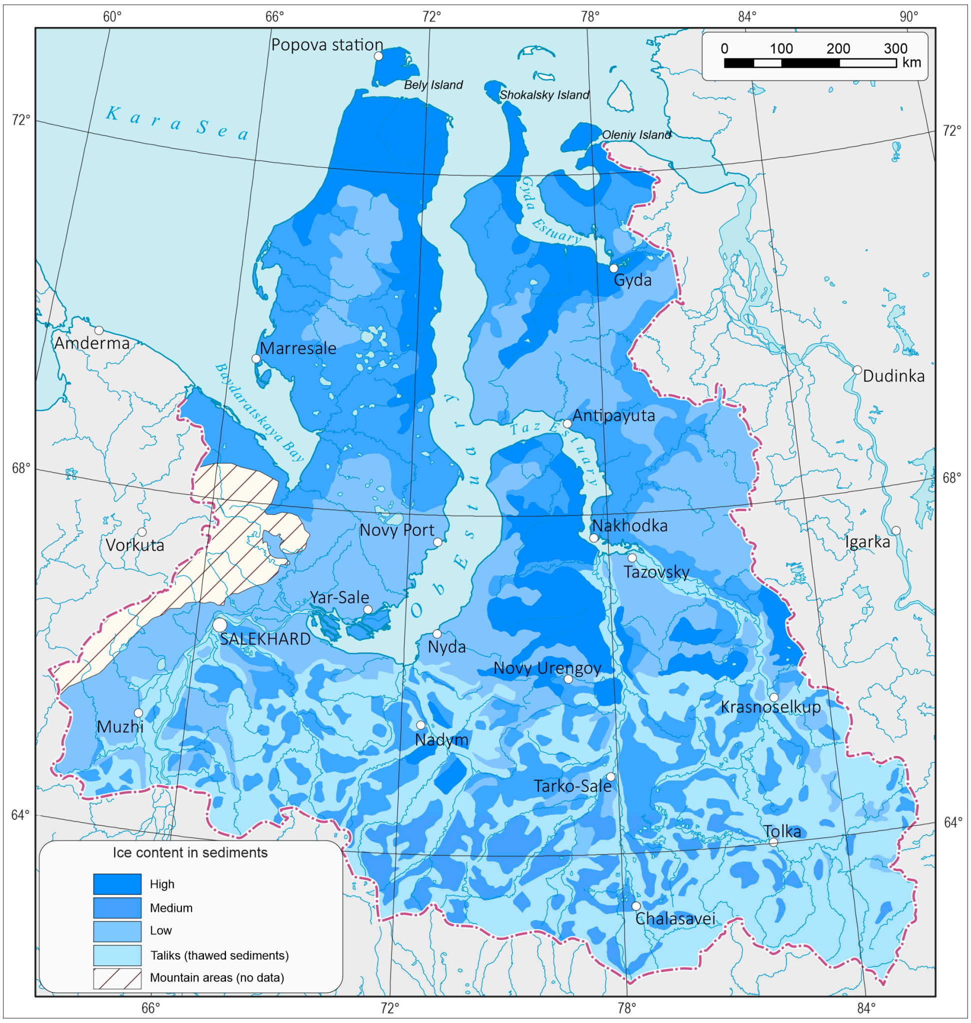

Figure 6. Volumetric ice content in the upper part of sediments in YaNAO by 2050: high—more than 50%; medium—from 30–50%; low—less than 30%.

4.9. Projection of Solifluction Phenomena under Climate Change

Solifluction is the slow flow of saturated soil downslope, indicating no frozen ground is present in the moving layer [55]. The shape of the slope, depth of thaw, and water content are significant factors affecting solifluction rates [18,56]. Solifluction develops most favorably on slopes of 5–20 degrees with a thickness of the thawed layer of 0.5–1 m.

The first step involved analyzing maps for landscapes, geological structure, ice content [46], and surface slope [47]. Satellite images were used to exclude floodplains, which were identified as flat and not subject to solifluction (now or in the future).

The next step involved calculating the thickness of the thawed layer ξ with a step of 1 degree, using the Kudryavtsev formula [57]:

$$\xi = \sqrt{\frac{\lambda \times T}{\pi \times C_v}} \times \xi*, \quad (7)$$

where $\xi* = \sqrt{(\sigma+\delta)^2+\delta} - \sigma$,

$$\delta = \ln\frac{\alpha+1}{\beta+1},\ \sigma = \frac{1}{2} \times \left[(\alpha-\beta) \times \left(1+\frac{1}{\delta}\right) - \delta \times \left(2+\frac{1}{\alpha-\beta}\right)\right],$$

$$\alpha = A_0 \times \frac{2 \times C_v}{L_v},\ \beta = |t_0| \times \frac{2 \times C_v}{L_v},\ C_v = \frac{C_{th} \times (A_0+t_0) + C_{f.} \times (A_0 - t_0)}{2 \times A_0},$$

λ—thermal conductivity (W/m·K), T—length of the year (hours), C_v—heat capacity (J/m^3·K), C_{th}—heat capacity in thawing soil (J/m^3·K), C_f—heat capacity in frozen soil (J/m^3·K), A_0—amplitude of temperature at the ground surface (°C), t_0—temperature at the ground surface(°C), L_v—heat of phase transition (W·h/m^3).

The condition for the solifluction occurrence is: $\tau > \tau_{long} + \sigma_{long}$, where τ—shear stress in thawing rocks, τ_{long}—long-term shear resistance of thawing rocks, σ_{long}—long-term rupture resistance of the vegetation cover. In the next step, to assess the possibility of solifluction, the minimum thickness of the seasonally thawed layer was calculated:

$$\xi_{min} = \frac{\tau_{long} + \sigma_{long}}{\gamma \times \sin\alpha \times \cos\alpha}, \quad (8)$$

γ—bulk density (kg/m^3),ξ—thickness of the thawed layer (m), α—slope angle (°).

Due to silty soils being most favorable for solifluction, the thickness of the seasonally thawed layer was calculated for this type of sediment. For convenience, the thermal conductivity in the thawed soil was equal to the thermal conductivity in the frozen. The input parameters used in the calculation are presented in Table 8.

Table 8. Soil properties used in the calculation.

Parameters	Water Content W		
	0.30	**0.45**	**0.60**
Soil density ρ, kg/m^3	1820	1740	1760
Bulk density γ, (kg/m^3)	1400	1200	1100
Heat capacity in thawing soil C_{th}, J/m^3·K	795	890	1010
Heat capacity in frozen soil C_f, J/m^3·K	555	580	625
Heat of phase transition L_v, W·h/m^3	38,976	44,544	56,144
Thermal conductivity λ, W/m·K	1.75	2.0	1.9
Shear resistance τ_{long}, (N/cm^2)	38	11	5.5

The YaNAO is characterized by various landscapes, with a predominance of different vegetation cover. The long-term rupture resistance of the vegetation cover was also different. For the moss-lichen cover of the northern and middle tundra σ_{long} = 15 N/cm^2; for the southern tundra and forest tundra σ_{long} = 25 N/cm^2; for the taiga σ_{long} = 45 N/cm^2.

At the next stage, the thematic maps of the factors that determine the solifluction processes and the results of grid calculations were compared, which made it possible to identify areas with different risks of solifluction under climate change (Figure 7). Finally, to project future solifluction rates under climate change, the values of air temperature and precipitation were analyzed. The solifluction rate was predicted to increase in areas with increasing air temperature and precipitation, which would lead to a thicker thawed layer and higher water content in the soil. The areas at the greatest risk of solifluction were identified based on a combination of slope, thaw depth, and water content, with areas of high slope and thick thawed layer being at the highest risk.

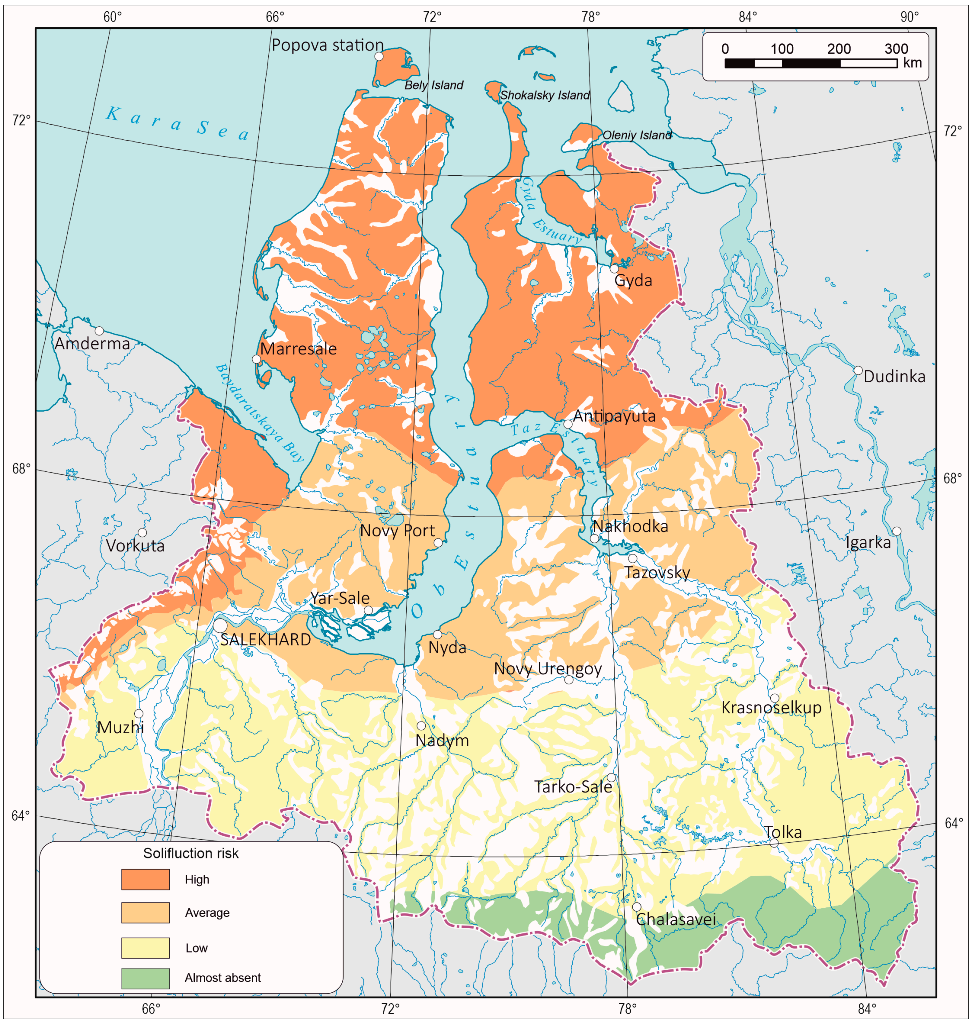

Figure 7. Intensity of solifluction in YaNAO by 2050: high risk—combination of more favorable factors for solifluction; average risk—some factors of solifluction are positive, but not all; low risk—unfavorable factors for solifluction are prevailing.

Calculations of the seasonally thawing minimum depth showed that for slopes with a steepness of more than 6° in the zone of the Arctic and middle tundra at a soil moisture content of 0.45 and 0.6, the critical thickness of the active layer will vary from 1.07 to 1.23 m. However, at current (by 2030) average annual air temperatures, individual values of the seasonally thawed layer are slightly higher, which does not correspond to the fulfillment of the necessary condition for the solifluction on slopes with a steepness of 6°. However, on slopes 8° or more, the condition is met. When soil moisture is 0.3, in order to comply with the condition for the solifluction occurrence, the slope steepness should be more than 10–12°, which corresponds to the minimum thickness of 1.43–1.7 m. The thickness of the seasonally thawing layer, calculated according to the Kudryavtsev formula, is greater than the critical depth for all predicted values by 2050. An increase in the slope's steepness up to 20° will be favorable for the solifluction when the thickness of 0.34–0.4 m for ice-rich soils and up to 0.84 m for icy soils (W = 0.3).

The predicted climate change by 2050, which is accompanied by an increase in the average annual temperature, is expected to increase the depth of seasonal thawing by 6–16% in the northern and central regions of the Yamal and Gydan Peninsulas, leading to solifluction due to the necessary conditions being met. Such areas are identified as high-risk areas on the map.

In the central part of YaNAO, corresponding to the southern tundra and forest-tundra zones, climate warming will cause an increase in the thickness of the seasonally thawing layer. If silty and sandy loams are present, this will be favorable for the development of solifluction. The minimum thickness of the seasonally thawing layer required for solifluction on icy soils is 2.0–2.5 m with a slope steepness of 8–10°, while for ice-rich soils, it is 1.6–1.8 m with a slope steepness of more than 6°. As a result, these areas are identified as high-risk areas for solifluction processes.

In the taiga zone to the south, solifluction decreases due to discontinuous permafrost distribution, wide distribution of forest vegetation, and a deep active layer. Solifluction is active only in areas without forest vegetation on the slope of northern exposure. Climate change is expected to lead to the degradation of permafrost and a decrease in solifluction processes, which will manifest locally and are shown as low risks or almost absent on the map.

4.10. Climate Change and Changes in the Area of Lakes

Overall, the distribution of lakes in a territory can be characterized by the lake area, which is calculated as the ratio of the total area of lake water surface to the area of the territory. For the YaNAO territory, the areas with a high lake cover percentage are those occupied by lakes of more than 7% [47]. According to the Boreal-Arctic Wetland and Lake Dataset, the average lake content within the YaNAO is 7.3% and reaches maximum values of 16–40% in the south of the YaNAO, in eastern Yamal and northern Gydan [58].

Climate warming in the permafrost zone may not necessarily lead to an increase in lake area. Instead, erosion and thermal denudation processes may cause some lakes to drain, leading to a decrease in lake area. This has been observed in the Arctic, where a negative surface water trend was seen during 2000–2021 [59]. While it was initially believed that climate change would cause lakes to grow due to the melting of ground ice, the reverse process can also occur due to the thawing of upper permafrost horizons, which leads to landscape transformation through the formation of drainage channels and intensified thermal erosion, ultimately leading to the drainage of lakes. The drainage of the Arctic occurs unevenly in continuous and discontinuous permafrost zones, with the most intensive drainage seen in the discontinuous permafrost zone. The maximum drying was observed in areas with high and medium ground ice content in permafrost, while areas with low ground ice content showed no significant changes in lake drainage despite a trend toward drying. Precipitation also plays a role in the drainage of lakes, with an increase in autumn precipitation leading to the degradation of permafrost and the drying of lakes due to rainwater contributing to the accelerated thawing of permafrost, the formation of runoff channels, and lake drainage [59].

Climate change in the coming decades can lead to both an increase in lake area (due to coastal erosion at large lakes and the growth of thermokarst lakes) and to lake drainage as a result of the mechanisms described above. At this stage, the greatest landscape changes can be reliably predicted in areas with high lake cover percentages and high or medium ground ice content in the upper horizons of the permafrost. For the lakes currently subjected to thermal denudation, an intensification of the thermal denudation process can be expected by 2050.

Based on data on lake cover percentage and ice content in the upper 10 m of the permafrost [47,59], a map of the lake area of the YaNAO was compiled, highlighting areas of high risk of lake geosystem changes. Areas with high lake cover percentages (7–16% and up to 40%) and medium to high ground ice content were classified as high-risk areas (Figure 8). For areas with an average lake cover percentage (0.5–2%), only areas with high ground ice content were classified as high-risk areas.

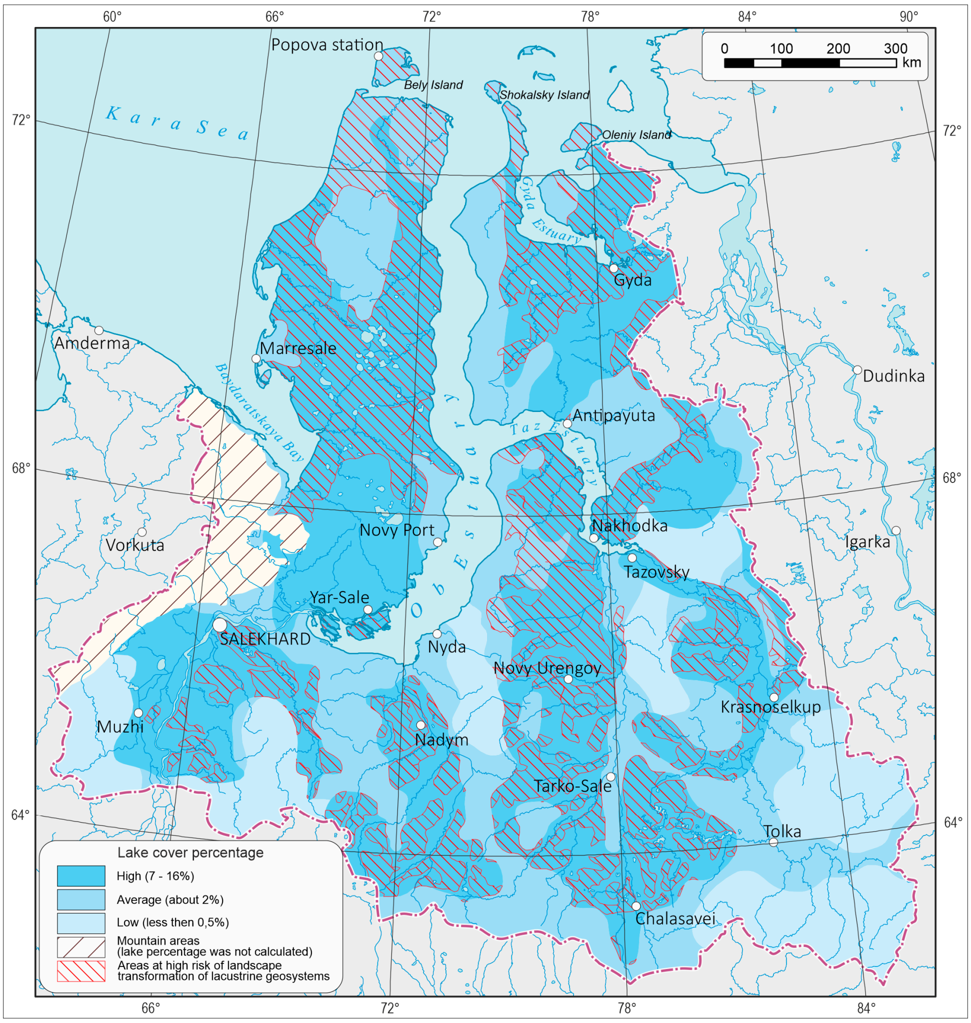

Figure 8. Lake area within YaNAO. Lake cover percentage based on [42,43]. The areas of high risk of transformation of lacustrine geosystems are drawn based on ice content in the upper layers of permafrost [47].

Undoubtedly, climatic changes will lead to the reshaping of lake-dominated geosystems. However, by 2050, the location of high-risk areas will be primarily determined by lake cover percentage and ice content in the upper part of the permafrost rather than climatic parameters. This is because the increase in summer temperatures within the high lake cover percentage areas of the YaNAO by 2050 will be fairly uniform, as will the overall increase in autumn precipitation.

4.11. Climate Change and Risks Connected with Karst

Karst is a destructive geomorphological process associated with water activity, resulting in the dissolution and leaching of rocks and the formation of peculiar landforms, such as karst sinkholes, saucers, caves, carr, fields, stalactites, stalagmites, and stalagnates. Karst processes and phenomena occur in areas composed of rocks that are relatively easily soluble in water, such as limestone, marble, gypsum, and rock salt. From a climatic perspective, karst processes are affected primarily by precipitation and temperature. Moisture is necessary for the dissolution of rocks, and higher air temperatures can accelerate the dissolution and washing out of rocks.

The Salekhard area is a unique place where one of the northernmost manifestations of karst processes occurs. A comprehensive analysis of climatic and geological data has revealed the intensity of these processes and associated risks.

To identify areas subject to karst processes, geological maps and schemes were processed and spatially referenced with respect to topographic maps and satellite images in the ArcGIS software package (ArcMap 10.4.1). The areas of distribution of karst rocks lying on the surface were delineated, and information on the degree of intensity of karst processes within these areas was collected from literature data and satellite images.

Data on the morphometric parameters of karst forms (craters, caves, etc.) and the composition and properties of karst rocks themselves were also analyzed. Changes in positive temperatures during the warm season and the amount of precipitation within the selected areas were also evaluated to assess possible changes in karst processes and the impact of climate change on karst processes within the YaNAO.

Overall, it was found that the intensity of predicted climate change is insufficient to significantly alter karst processes. Risks associated with karst processes are present only to the northwest of Salekhard, where folded structures of the Ural Mountain belt come to the surface, and limestones and dolomites of the Paleozoic can be subjected to karst processes.

The Yanganape Range, located in the Ural region, is the most active area for karst processes. It is a natural monument where some of the world's northernmost karst caves can be seen. The massif consists of three flat peaks, with the highest point being 293 m on the southwestern peak. The ridges are ancient reefs of the Lower Devonian age, formed in the Late Devonian within the ancient island arcs of the paleooceanic sector of the Ural mobile belt. The reefs vary in shape and size, with symmetrical slopes, and have diameters of 0.5–1 km. The presence of caves up to a few tens of meters long, with an entrance width of more than 3 m, with grottoes, branches, and halls, makes the area of the Yanganape Ridge classified as an area with a dangerous level of development of karst processes. The area is home to several caves, including Chernetsova and Akademicheskaya, which are known for being the northernmost karst objects in the world, where zoogenic deposits were found. The Yanganape Ridge also features a karst lake that is 36 m deep on its top surface. Due to the unique karst landscapes and the karst lake with the purest water, which is considered sacred by the Nenets, it is preferable to classify the Yanganape Ridge as a natural monument, part of a nature reserve, or national park with a ban on construction and industrial activity within its boundaries.

The presence of caves up to a few tens of meters long, with an entrance width of more than 3 m, with grottoes, branches, and halls make it possible to classify the area of the Yanganape Ridge as an area with a dangerous level of development of karst processes. Given the unusual nature of its karst landscapes and a karst lake with the purest water, which is considered sacred by the Nenets, it is preferable to single it out as a natural monument, part of a nature reserve or national park with a ban on construction and industrial activity within its boundaries. This is the only area in the West Siberian North where karst processes can be considered relatively dangerous for economic activity. The remaining distribution areas of karst rocks were classified as moderately hazardous areas, primarily limestone outcrops and worse than karst dolomites, marbled limestones, and marbles.

In general, under the conditions of a short northern summer at low positive temperatures, karst processes proceed with low intensity. Karst processes in the region are less sensitive to climate change than other dangerous geomorphological processes. Although the climate changes expected by the middle of the 21st century may somewhat affect the speed of karst processes in the direction of their acceleration due to an increase in temperature, the intensity of the processes will be insignificant and will not have a large impact on the degree of risks associated with karst processes.

4.12. Climate Change and Risks Connected with Frost Heave

Soil frost heaving is a dangerous geomorphological process associated with the formation of frost heave mounds-positive forms with an ice core resulting from uneven freezing and ice formation in fine-grained deposits. Frost mounds are formed in areas composed of permafrost, both in continuous and discontinuous permafrost zones. They can be formed with the participation of groundwater inflow (open-system pingo), in the place of taliks under former lakes, or simply in relatively water-saturated soils when a closed volume of soil freezes. They can also form as segregated ice, growing towards the freezing front.

To study the heaving process, literature data on the frequency, morphology, occurrence, and distribution areas of frost mounds, as well as the morphometric parameters of frost mounds, the growth rate, and features of this permafrost process, were used. To analyze the current state and risks associated with heaving, frost mounds were identified on topographic maps and satellite images. The frequency of their occurrence, the number of frost mounds per unit area, size, and shape were analyzed. Permafrost distribution and properties that affect heaving were also analyzed.

It was revealed which meteorological parameters affect the heaving process. Heaving is especially noticeable during a long period of slow temperature decrease (at negative temperatures not lower than $-0.3 \div -0.5$ °C), sufficient for the growth of ice crystals, which increase the volume of freezing water, and, consequently, the soil [60]. The amount of soil moisture, especially free water, in freezing sediments affects heaving and, of course, in the presence of frost-susceptible soils. Thus, from the meteorological parameters, the amount of precipitation and air temperature in the spring and autumn months is important: the longer the freezing period is, and the more transitions through 0 °C during the year, the stronger the heaving process occurs.

The step-by-step scheme for assessing the heaving of soils was as follows: at the first stage, the current distribution of frost mounds was estimated using satellite images and topographic maps. Maps of the intensity of heaving risks at the present stage were constructed. Numerical values, such as the susceptibility of the territory to heaving and the area where heaving is distributed over more than 25% of the territory, were calculated using data on the distribution of frost mounds taken from maps and space images and their growth rate was assumed based on the density and morphometric parameters. In addition, when constructing maps, data on the composition of soils were used, which was estimated from geological and geomorphological maps. The parameters of permafrost, on which the mechanisms of the heaving process largely depend, were also taken into account: areas with a continuous permafrost distribution, where heaving can occur at certain levels everywhere, and discontinuous distribution of permafrost, where it occurs only within permafrost islands, were identified on the map.

In the second stage, when the forecast was made for 2050, the location of the zones with the greatest risk was calculated, taking into account future changes in temperature and humidity, which would be superimposed on the existing pattern of heaving intensity. Maps of changes in air temperature and humidity in the summer, autumn, and spring months were superimposed on the map of modern risks associated with heaving, and a forecast was made by the method of expert assessment of how the intensity of heaving processes would change. The assessment included an estimation of how the zones of maximum hazard will move if the temperature increases and permafrost degrades in the south on the one hand and becomes less stable in the north on the other hand.

It was revealed that heaving processes can manifest themselves to varying degrees throughout the entire area of YaNAO, wherever there are fine-grained permafrost deposits. However, there are both areas where risks will be small and areas with high risks (Figure 9).

Currently, the greatest risks associated with frost mounds are observed in the central part of the Yamal Peninsula, as well as in the northern part of the Tazovskiy Peninsula. The highest concentration of frost mounds per unit area is noted here. The rate of development of frost mounds can be different, with fluctuations in growth and degradation. The maximum rate of growth can reach 5–10 cm/year. The sizes of frost mounds range from 0.5 m in height and 0.5–1 m in diameter to rather large ones, up to 6–7 m high and up to 15–20 m in diameter on average in the Yamal region. Such frost mounds are found in places of their greatest concentration: in the area to the east along the Marresale polar station, in the Seyakha settlement area, on the Taz Peninsula, etc.

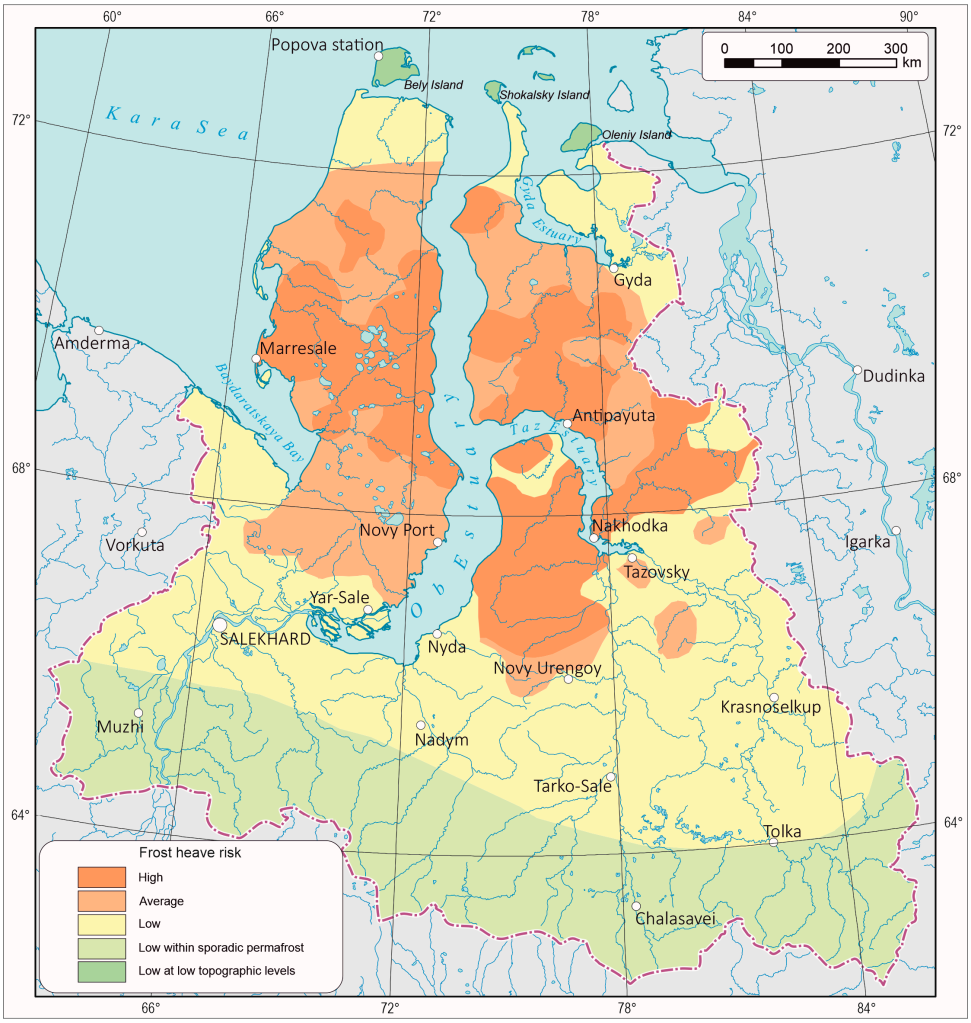

Figure 9. Frost heave risk by 2050: areas most vulnerable to frost heave risk are shown in red color.

According to the hazard assessment of the frost mounds, on average, the risks in such areas could be assessed as moderately dangerous or dangerous, but there is another factor associated with the frost mounds, which allows us to classify the areas of their maximum concentration within gas fields and areas of gas manifestations as very dangerous. This is a recently discovered phenomenon of the formation of so-called gas emission funnels at the site of frost mounds [61]. There are various theories about the origin of the explosions themselves and the formation of craters. However, at the moment, there is a consensus that the gas emission funnel is a natural stage in the development of frost mounds with a gas-saturated ice core. Such funnels tend to occur in the site of frost mounds and often in areas of gas manifestation. Since the explosion of a frost mound can be extremely dangerous for structures and infrastructure, areas with an increased concentration of mounds within gas-bearing structures were identified on the maps as very dangerous areas.

On average, the central part of the YaNAO area is the most prone to frost mounds. To the north, in the area at the tip of Bely Island, frost mounds will occur mainly in low-lying areas. Here, low-temperature permafrost will still be preserved, which thaws little over the summer, and there will be almost no drainage and degradation of lakes. As a result, there will be no areas of thawed soil that can freeze through from all sides, leading to frost mounds. Such processes will occur only on low sea terraces and in river valleys where taliks are present, and frost mounds are unlikely on the summit surfaces.

In southern regions, the formation of frost mounds is possible, but it will not be as active as in the center of Yamal and Gydan. In areas with discontinuous permafrost, heaving will occur within permafrost islands, and it will be especially active within swamps and peat bogs.

By 2050, as a result of increasing air temperatures and permafrost degradation, heaving processes are expected to become more active. In general, the heaving process often accompanies permafrost degradation. Warming occurs in steps, with thawing alternating with freezing. As temperatures rise, taliks can form. With subsequent temporary cooling, these taliks can freeze in a closed volume, forming mounds. This process can be repeated many times over several years, posing a threat to structures and infrastructure. An increase in the number of frost mounds and an increase in the risks associated with this process are expected in the areas of greatest risk, such as Marresale and Seyakha. As permafrost continues to degrade, new funnels of gas emission may appear.

In addition, all borders shown on the map of the current situation are expected to shift northward. The border of discontinuous permafrost will move northward, and the area with the highest risk of heaving will cover the northern parts of the Yamal and Gydan peninsulas. On Bely Island and other Arctic islands in the interfluves, low-temperature permafrost will still be present and will not yet thaw with subsequent heaving and freezing of taliks. However, heaving will become even more active on low surfaces in these areas.

5. Conclusions

Overall, the distribution of predicted anomalies of temperature and precipitation is relatively homogeneous across the YaNAO due to the area's size and flat terrain. However, changes in the state of the environment are more complex and mosaic, influenced by factors such as soil properties, coastline configuration, and landforms. Processes directly controlled by air temperature and precipitation will have the greatest response in mountainous regions, such as avalanches and slush flows.

The parameters of environmental change triggered by climate change were based on predicted temperature and precipitation data using simple algorithms for calculations. The use of complex schemes is deemed unproductive due to significant uncertainties associated with both the climate forecast and the unreliability of information on the spatial and temporal characteristics of soils.

Climate change causes changes in the Arctic environment, primarily due to permafrost degradation, which is sensitive to changes in air temperature and precipitation, leading to a change in the activity of certain exogenous processes. In some cases, the intensity and area of these processes increase, such as heaving processes and thermokarst becoming more active by 2050 due to an increase in ground temperature and the depth of seasonal thawing. In other cases, processes associated with permafrost transformation may fade due to its complete or partial disappearance, as in the taiga zone to the south, where solifluction processes decrease due to the discontinuous or sporadic permafrost distribution.

Processes for which permafrost dynamics is not decisive proceed much more slowly. For example, the nature of the karst process is less sensitive to climate change, and thus a significant change in karst processes by the middle of the 21st century cannot be expected. Based on meteorological data analysis, it was found that by 2050, the activity of karst processes and the associated risks will practically not change compared to the current state.

Projected climatic changes will inevitably lead to the restructuring of the geosystems in YaNAO, creating risks for infrastructure. These risks should be considered in the development of a plan for adapting the YaNAO region to climate change.

Author Contributions: Conceptualization, A.K.; Data curation, A.B., N.B., D.B., M.V. and I.Z.; Formal analysis, A.K. and G.S.; Investigation, A.K., A.B., N.B., D.B. and M.V.; Methodology, A.K.; Resources, A.B., N.B., D.B., M.V. and I.Z.; Software, I.Z.; Supervision, A.K.; Validation, I.Z.; Visualization, A.A.; Writing—original draft, A.B., N.B., D.B., G.S. and M.V.; Writing—review & editing, A.K., A.A., A.B., N.B., D.B. and M.V. All authors have read and agreed to the published version of the manuscript.

Funding: The research of A. Kislov and I. Zheleznova was funded by the Russian Geographical Society (the Moscow branch), contract number 122 (2022). The research of N. Belova and D. Bogatova was funded by the Russian Science Foundation (RSF) grant number 22-17-00097. The research of A. Baranskaya on thermal abrasion and frost heave was funded by the Russian Science Foundation (RSF) grant number 22-77-10031. The research of G. Surkova was funded by the Program of the Interdisciplinary Scientific and Educational School of Lomonosov Moscow State University, "The Future of the Planet and Global Environmental Changes". The research of A. Alyautdinov and M. Vikulina was funded by the Program of Lomonosov Moscow State University (#121051100164-0).

Data Availability Statement: General data used in this study is archived in the repository (Datasets Generated: "Mendeley Data", https://data.mendeley.com/v1/datasets/5s7hj98ft8/draft?preview=1 accessed on 26 February 2023).

Conflicts of Interest: The authors declare that they have no known competing financial interests or personal relationships that could have appeared to influence the work reported in this paper.

References

1. Serreze, M.C.; Barry, R.G. Processes and Impacts of Arctic Amplification: A Research Synthesis. *Glob. Planet. Change* **2011**, *77*, 85–96. [CrossRef]
2. Cohen, J.; Screen, J.A.; Furtado, J.C.; Barlow, M.; Whittleston, D.; Coumou, D.; Francis, J.; Dethloff, K.; Entekhabi, D.; Overland, J.; et al. Recent Arctic Amplification and Extreme Mid-Latitude Weather. *Nat. Geosci.* **2014**, *7*, 627–637. [CrossRef]
3. Ye, K.; Wu, R.; Liu, Y. Interdecadal Changes of Eurasian Snow, Surface Temperature and Atmospheric Circulation in the Late 1980s. *J. Geophys. Res. Atmos.* **2015**, *120*, 2738–2753.
4. Polyakov, I.V.; Pnyushkov, A.V.; Alkire, M.B.; Ashik, I.M.; Baumann, T.M.; Carmack, E.C.; Goszczko, I.; Guthrie, J.; Ivanov, V.V.; Kanzow, T.; et al. Greater role for Atlantic inflows on sea-ice loss in the Eurasian Basin of the Arctic Ocean. *Science* **2017**, *356*, 285–291. [CrossRef]
5. Screen, J.; Simmonds, I. The central role of diminishing sea ice in recent Arctic temperature amplification. *Nature* **2010**, *464*, 1334–1337. [CrossRef]
6. Riihelä, A.; Bright, R.M.; Anttila, K. Recent strengthening of snow and ice albedo feedback driven by Antarctic sea-ice loss. *Nat. Geosci.* **2021**, *14*, 832–836. [CrossRef]
7. Shabanov, P. Changes in the Ice-Free Period Duration in the Kara Sea Coastal Zone from Satellite Data. *Oceanology* **2022**, *62*, 447–457. [CrossRef]
8. Kislov, A.; Matveeva, T.; Antipina, U. Precipitation Extremes and Their Synoptic Models in the Northwest European Sector of the Arctic during the Cold Season. *Atmosphere* **2022**, *13*, 1116. [CrossRef]
9. Kislov, A.; Antipina, U.I.; Korneva, I.A. Precipitation extrema over the European sector of the Arctic during the summer time: Statistics and synoptic models. *Russ. Meteorol. Hydrol.* **2012**, *46*, 434–443. [CrossRef]
10. Agafonova, S.A.; Frolova, N.A.; Surkova, G.V.; Koltermann, K.P. Modern characteristics of the ice regime of Russian arctic rivers and their possible changes in the 21st century. *Geogr. Environ. Sustain.* **2017**, *10*, 4–15. [CrossRef]
11. Perov, V.; Chernomorets, S.; Budarina, O.; Savernyuk, E.; Leontyeva, T. Debris flow hazards for mountain regions of Russia: Regional features and key events. *Nat. Hazards* **2017**, *88*, 199–235. [CrossRef]
12. Ramage, J.L.; Irrgang, A.M.; Herzschuh, U.; Morgenstern, A.; Couture, N.; Lantuit, H. Terrain controls on the occurrence of coastal retrogressive thaw slumps along the Yukon Coast, Canada. *J. Geophys. Res. Earth Surf.* **2017**, *122*, 1619–1634. [CrossRef]
13. Shabanova, N.N.; Ogorodov, S.; Shabanov, P.; Baranskaya, A. Hydrometeorological forcing of Western Russian arctic coastal dynamics: XX-century history and current state. *Geogr. Environ. Sustain.* **2018**, *11*, 113–129. [CrossRef]
14. Irrgang, A.M.; Bendixen, M.; Farquharson, L.M.; Baranskaya, A.V.; Erikson, L.H.; Gibbs, A.E.; Ogorodov, S.A.; Overduin, P.P.; Lantuit, H.; Grigoriev, M.N.; et al. Drivers, dynamics and impacts of changing Arctic coasts. *Nat. Rev. Earth Environ.* **2022**, *3*, 39–54. [CrossRef]
15. Bennett, S.; Wells, R. Gully erosion processes, disciplinary fragmentation, and technological innovation. *Earth Surf. Process. Landf.* **2019**, *44*, 46–53. [CrossRef]
16. Fell, R.; Fry, J.-J. *Internal Erosion of Dams and Their Foundations*; Taylor & Francis: London, UK, 2007.
17. Badu, Y.B.; Nikitin, K.A. Frost mounds within the gas-bearing structures, northern part of Western Siberia. *Earth's Cryosphere* **2020**, *24*, 17–26.
18. Hjort, J.; Ujanen, J.; Parviainen, M.; Tolgensbakk, J.; Etzelmüller, B. Transferability of geomorphological distribution models: Evaluation using solifluction features in subarctic and Arctic regions. *Geomorphology* **2014**, *204*, 165–176. [CrossRef]
19. Dixon, J.C. Response of periglacial geomorphic processes to global change. In *Treatise on Geomorphology*; Shroder, J., James, L.A., Harden, C.P., Clague, J.J., Eds.; Geomorphology of Human Disturbances, Climate Change, and Natural Hazards; Academic Press: San Diego, CA, USA, 2013; Volume 13, pp. 176–189.
20. Eyring, V.; Bony, S.; Meehl, G.A.; Senior, C.A.; Stevens, B.; Stouffer, R.J.; Taylor, K.E. Overview of the Coupled Model Intercomparison Project Phase 6 (CMIP6) experimental design and organization. *Geosci. Model Dev.* **2016**, *9*, 1937–1958. [CrossRef]

21. Hersbach, H.; Bell, B.; Berrisford, P.; Biavati, G.; Horanyi, A.; Sabater, J.; Nicolas, J.; Peubey, C.; Radu, R.; Rozum, I.; et al. ERA5 Hourly Data on Single Levels from 1959 to the Present. Copernicus Climate Change Service (C3S) Climate Data Store (CDS). 2018. Available online: https://cds.climate.copernicus.eu/cdsapp#!/dataset/reanalysis-era5-single-levels?tab=overview (accessed on 1 January 2020).
22. La Laternser, M.; Schneebeli, M. Temporal Trend and Spatial Distribution of Avalanche Activity during the Last 50 Years in Switzerland. *Nat. Hazards* **2002**, *27*, 201–230. [CrossRef]
23. Eckert, N.; Lavigne, A.; Castebrunet, H.; Giraud, G.; Naaim, M. Recent changes in avalanche activity in the French Alps and their links with climatic drivers: An overview. In Proceedings of the International Snow Science Workshop 2013, Grenoble, France, 7–11 October 2013; pp. 1211–1215.
24. Valt, M.; Cianfarra, P. Recent Variability of Avalanche Activity and Snowfall in the Italian Alps. *Cold Reg. Sci. Technol.* **2010**, *64*, 146–157. [CrossRef]
25. Glazovskaya, T.G. Global distribution of snow avalanches and changing activity in the Northern Hemisphere due to climate change. *Ann. Glaciol.* **1998**, *26*, 337–342. [CrossRef]
26. Hungr, O.; Evans, S.G.; Bovis, M.; Hutchinson, J.N. Review of the classification of landslides of the flow type. *Environ. Eng. Geosci.* **2001**, *7*, 221–238. [CrossRef]
27. Hestnes, E. Slushflow hazard—Where, why and when? 25 years of experience with slushflow consulting and research. *Ann. Glaciol.* **1998**, *26*, 370–376. [CrossRef]
28. Lewkowicz, A.G.; Way, R.G. Extremes of summer climate trigger thousands of thermokarst landslides in a high Arctic environment. *Nat. Commun.* **2019**, *10*, 1329. [CrossRef] [PubMed]
29. Hayes, S.; Lim, M.; Whalen, D.; Mann, P.J.; Fraser, P.; Penlington, R.; Martin, J. The role of massive ice and exposed headwall properties on retrogressive thaw slump activity. *J. Geophys. Res. Earth Surf.* **2022**, *127*, e2022JF006602. [CrossRef]
30. Nesterova, N.B.; Khomutov, A.V.; Leibman, M.O.; Safonov, T.A.; Belova, N.G. The inventory of retrogressive thaw slumps (thermocirques) in the north of West Siberia based on 2016–2018 satellite imagery mosaic. *Earth's Cryosphere* **2021**, *25*, 34–41. [CrossRef]
31. Günther, F.; Overduin, P.P.; Sandakov, A.V.; Grosse, G.; Grigoriev, M.N. Short- and long-term thermo-erosion of ice-rich permafrost coasts in the Laptev Sea region. *Biogeosciences* **2013**, *10*, 4297–4318. [CrossRef]
32. Ogorodov, S.; Baranskaya, A.; Belova, N.; Kamalov, A.; Kuznetsov, D.; Overduin, P.; Shabanova, N.; Vergun, A. Coastal dynamics of the Pechora and Kara seas under changing climatic conditions and human disturbances. *Geogr. Environ. Sustain.* **2016**, *9*, 53–73. [CrossRef]
33. Ogorodov, S.A.; Shabanova, N.N.; Kessel, A.S.; Baranskaya, A.V.; Razumov, S.O. Changes of the hydrometeorological potential of thermoabrasion on the Russian Arctic sea coasts. *Vestnik Moskovskogo Universiteta Seriya 5 Geografiya* **2022**, *1*, 26–42. (In Russian)
34. Novikova, A.; Belova, N.; Baranskaya, A.; Aleksyutina, D.; Maslakov, A.; Zelenin, E.; Shabanova, N.; Ogorodov, S. Dynamics of permafrost coasts of Baydaratskaya Bay (Kara Sea) based on multi-temporal remote sensing data. *Remote Sens.* **2018**, *10*, 1481. [CrossRef]
35. Aleksyutina, D.M.; Shabanova, N.N.; Kokin, O.V.; Vergun, A.P.; Novikova, A.V.; Ogorodov, S.A. Monitoring and modelling issues of the thermoabrasive coastal dynamics. *IOP Conf. Ser. Earth Environ. Sci.* **2018**, *193*, 012003. [CrossRef]
36. Günther, F.; Overduin, P.P.; Yakshina, I.A.; Opel, T.; Baranskaya, A.V.; Grigoriev, M.N. Observing Muostakh disappear: Permafrost thaw subsidence and erosion of a ground-ice-rich island in response to arctic summer warming and sea ice reduction. *Cryosphere* **2015**, *9*, 151–178. [CrossRef]
37. Baranskaya, A.; Novikova, A.; Shabanova, N.; Romanenko, F.; Ogorodov, S. Late Quaternary and modern evolution of permafrost coasts at Beliy island, Kara Sea. *J. Coast. Res.* **2020**, *95*, 356–361. [CrossRef]
38. Kritsuk, L.N.; Dubrovin, V.A.; Yastreba, N.V. Some results of integrated study of the Kara Sea coastal dynamics in the Marre-Sale meteorological station area, with the use of GIS technologies. *Earth's Cryosphere* **2014**, *18*, 59–69.
39. Belova, N.G.; Shabanova, N.N.; Ogorodov, S.A.; Baranskaya, A.V.; Novilova, A.V. Coastal Erosion at Kharasavey Gas Condensate Field, Western Yamal Peninsula. In Proceedings of the 2018 SPE Russian Petroleum Technology Conference, RPTC 2018, Moscow, Russia, 15–17 October 2018.
40. Baranskaya, A.; Novikova, A.; Shabanova, N.; Belova, N.; Maznev, S.; Ogorodov, S.; Jones, B.M. The role of thermal denudation in erosion of ice-rich permafrost coasts in an enclosed bay. *Front. Earth Sci.* **2021**, *8*, 566227. [CrossRef]
41. Belova, N.; Ermolov, A.; Novikova, A.V.; Ogorodov, S.; Stanilovskaya, Y. Dynamics of low-lying sandy coast of the Gydan peninsula, Kara Sea, Russia, based on multi-temporal remote sensing data. *Remote Sens.* **2023**, *15*, 48. [CrossRef]
42. Belova, N.G.; Novikova, A.V.; Günther, F.; Shabanova, N.N. Spatiotemporal variability of coastal retreat rates at Western Yamal peninsula, Russia, based on remotely sensed data. *J. Coast. Res.* **2020**, *95*, 367–371. [CrossRef]
43. Golay, F.; Bonelli, S. Numerical modelling of suffusion as an interfacial erosion process. *Eur. J. Environ. Civ. Eng.* **2011**, *15*, 1225–1241. [CrossRef]
44. Khomenko, V.P. *Patterns and Forecast of Suffusion Processes*; GEOS: Moscow, Russia, 2003. (In Russian)
45. Gutierrez, F.; Guerrero, J.; Lucha, P. A genetic classification of sinkholes illustrated from evaporate paleokarst exposures in Spain. *Environ. Geol.* **2008**, *53*, 993–1006. [CrossRef]
46. Baulin, V.V. (Ed.) *Map of geocryological zoning of the West Siberian Plain according to the upper horizon of the permafrost. Scale 1:1, 500,000 Million*; State Cartographic Factory: Moscow, Russia, 1982. (In Russian)

47. Larin, S.I. (Ed.) *Atlas of the Yamalo-Nenets Autonomous Area*; Federal State Unitary Enterprise Omsk Cartographical Factory: Omsk, Russia, 2004. (In Russian)
48. Chen, L.; Zhang, H.Y.; Lei, W.; Liang, Y.; Ji, C.; Wang, C. Piping and non-uniform permeability development of cohesionless soils. *Chin. J. Geotech. Eng.* **2012**, *34*, 1432–1439.
49. Strokova, L.A.; Epifanova, E.A. Assessment of suffosion in the territory of settlement Sabetta, the Yamal Peninsula. *Bull. Tomsk. Polytech. Univ. Geo Assets Eng.* **2021**, *332*, 95–106. (In Russian)
50. Sidorchuk, A. The Potential of Gully Erosion on the Yamal Peninsula, West Siberia. *Geogr. Environ. Sustain.* **2020**, *12*, 260. [CrossRef]
51. Bogatova, D.; Baranskaya, A.; Belova, N.; Ogorodov, S. The role of permafrost processes in the coastal dynamics of the Kara Sea. In Proceedings of the 26th International Conference on Port and Ocean Engineering under Arctic Conditions, Moscow, Russia, 14–18 June 2021.
52. Sannikov, G.S. Cartometric research of thermokarst lakes within the Bovanenkovo gas field territory, Yamal peninsula. *Earths Cryosphere* **2012**, *16*, 30–37. (In Russian)
53. Wei, Y.; Wu, X.; Cai, C. Splash erosion of clay-sand mixtures and its relationship with soil physical properties: The effects of particle size distribution on soil structure. *Catena* **2015**, *135*, 254–262. [CrossRef]
54. Badu, Y.B.; Gafarov, E.A.; Podborny, E.E. (Eds.) Cryosphere Bovanenkovo gas condensate fields. In *Cryosphere Gas Condensate Fields on the Yamal Peninsula*; Gazprom Ekspo: Moscow, Russia, 2013. (In Russian)
55. Washburn, A.L. *Geocryology*; Edward Arnold: London, UK, 1979; Volume 117, pp. 503–504.
56. Walker, H.J. Periglacial environments. In *A Handbook of Engineering Geomorphology*; Fookes, P.G., Vaughan, P.R., Eds.; Chapman and Hall: New York, NY, USA, 1986; pp. 82–96.
57. Kudryavtsev, V.A. (Ed.) *Basics of Permafrost Forecast in Engineering-Geological Investigations*; Moscow University Press: Moscow, Russia, 1974. (In Russian)
58. Olefeldt, D.; Hovemyr, M.; Kuhn, A.; Bastviken, D.; Bohn, T.J.; Connolly, J.; Crill, P.; Euskirchen, E.S.; Finkelstein, S.A.; Genet, H.; et al. The boreal-arctic wetland and lake dataset (BAWLD). *Earth Syst. Sci. Data* **2021**, *13*, 5127–5149. [CrossRef]
59. Webb, E.E.; Liljedahl, A.K.; Cordeiro, J.A.; Loranty, M.M. Permafrost thaw drives surface water decline across lake-rich regions of the Arctic. *Nat. Clim. Change* **2022**, *12*, 841–846. [CrossRef]
60. Vasil'chuk, Y.; Chizhova, J.; Budantseva, N.; Kurchatova, A.; Rogov, V.; Vasil'chuk, A. Stable oxygen and hydrogen isotope compositions of the Messoyakha and Pestsovoe pingos in northwest Siberia as markers of ice core formation. *Permafr. Periglac. Process.* **2021**, *32*, 558–571. [CrossRef]
61. Dvornikov, Y.A.; Leibman, M.O.; Khomutov, A.V.; Kizyakov, A.I.; Semenov, P.B.; Bussmann, I.; Babkin, E.M.; Heim, B.; Portnov, A.; Babkina, E.A.; et al. Gas-emission craters of Yamal and Gydan peninsulas: A proposed mechanism for lake genesis and development of permafrost landscapes. *Permafr. Periglac. Process.* **2019**, *30*, 146–162. [CrossRef]